J. Fluid Mech. (2018), *vol.* 853, *pp.* 386–418.
doi:10.1017/jfm.2018.568

Saturation of a turbulent mixing layer over a cavity: response to harmonic forcing around mean flows

E. Boujo[1,†], **M. Bauerheim**[1] **and N. Noiray**[1,†]

[1]CAPS Lab, Mechanical and Process Engineering Department, ETH Zürich, CH-8092 Zürich, Switzerland

(Received 31 October 2017; revised 18 May 2018; accepted 17 July 2018; first published online 23 August 2018)

Turbulent mixing layers over cavities can couple with acoustic waves and lead to undesired oscillations. To understand the nonlinear aspects of this phenomenon, a turbulent mixing layer over a deep cavity is considered and its response to harmonic forcing is analysed with large-eddy simulations (LES) and linearised Navier–Stokes equations (LNSE). The Reynolds number is $Re = 150\,000$. As a model of incoming acoustic perturbations, spatially uniform time-harmonic velocity forcing is applied at the cavity end, with amplitudes spanning the wide range 0.045–8.9 % of the main channel bulk velocity. Compressible LES provide reference nonlinear responses of the shear layer, and the associated mean flows. Linear responses are calculated with the incompressible LNSE around the LES mean flows; they predict well the amplification (both measured with kinetic energy and with a proxy for vortex sound production in the mixing layer) and capture the nonlinear saturation observed as the forcing amplitude increases and the mixing layer thickens. Perhaps surprisingly, LNSE calculations based on a monochromatic (single-frequency) assumption yield a good agreement even though higher harmonics and their nonlinear interaction (Reynolds stresses) are not negligible. However, it is found that the leading Reynolds stresses do not force the mixing layer efficiently, as shown by a comparison with the optimal volume forcing obtained from a resolvent analysis. Therefore they cannot fully benefit from the potential for amplification available in the flow. Finally, the sensitivity of the optimal harmonic forcing at the cavity end is computed with an adjoint method. The sensitivities to mean flow modification and to a localised feedback (structural sensitivity) both identify the upstream cavity corner as the region where a small-amplitude modification has the strongest effect. This can guide in a systematic way the design of strategies aiming at controlling the amplification and saturation mechanisms.

Key words: acoustics, instability, turbulent flows

1. Introduction

Flow over a cavity leads to a variety of interesting phenomena, including radiated noise in the form of broadband and discrete components. Related applications are

† Email addresses for correspondence: eboujo@ethz.ch, noirayn@ethz.ch

numerous in aeronautics (wheel wells), ground transportation (pantograph cavities, door gaps, open windows), turbomachinery (bleed slots for secondary air supply in compressors) and other energy-related systems (T-junctions and side branches in pipe networks for air, water, steam or gas). Therefore, it comes as no surprise that, for more than 60 years, many studies have investigated cavity flows. In general, sustained vortical oscillations in the shear layer and acoustic oscillations result from a process involving hydrodynamics and acoustics, although the details depend on the specific configuration (see for instance reviews by Rockwell & Naudascher 1978, 1979; Rockwell 1983; Rowley & Williams 2006; Morris 2011; Tonon *et al.* 2011). In shallow cavities (width-to-height aspect ratio $W/H \gtrsim 1$), vortical disturbances in the shear layer impinge on the downstream cavity corner, and cavity tones may be generated by a feedback mechanism (hydrodynamic/acoustic feedback in incompressible/compressible flows at small/large Mach number). In deep cavities (aspect ratio $W/H \lesssim 1$), resonant pipe tones may be generated if a cavity acoustic mode (standing wave) is excited by the shear layer (turbulence-induced broadband excitation and/or instability-induced narrowband excitation).

Many linear models have been developed for predicting oscillation frequencies (Rossiter 1964; Tam & Block 1978; Alvarez, Kerschen & Tumin 2004; Kooijman, Golliard & Hirschberg 2004). However, accounting for nonlinear saturation and predicting oscillation amplitude remains a challenge. Full Navier–Stokes simulations are computationally expensive, especially in the turbulent regime, and simpler methods are still few. Rowley & Williams (2006) mention a model by Cain *et al.* (1996) which 'assumes oscillations at the Rossiter frequencies, and assumed nonlinearities enter through saturation of the shear layer: as the amplitude of oscillation grows, Reynolds stresses increase, and the shear layer spreads, decreasing the amplification rate of disturbances. The total amplification of a disturbance is computed around the loop, and an iterative procedure is used to converge to the final oscillation amplitude'. Because this procedure assumes specific nonlinearities, it may be too simplified to give accurate predictions in a wide range of conditions; however, its description of the saturation mechanism is particularly interesting because it probably captures the key ingredients at play. It also points to a recent study by Mantič-Lugo & Gallaire (2016) who used a related description for predicting the hydrodynamic response to harmonic forcing in the laminar flow over a backward-facing step. Their model is a system of two equations: the response to harmonic forcing at frequency ω_1 is given by a linear equation (Navier–Stokes operator linearised around the mean flow), while nonlinear interaction of the response with itself modifies the mean flow. As nonlinear saturation effects increase, the mean flow and the linear response progressively converge (both in the iterative algorithm and in the physical flow) to a steady regime. In this semi-linear self-consistent model, the only assumption is that higher harmonics can be neglected altogether, i.e. they have no effect on the linear response at ω_1, nor on the mean flow correction.

In this paper we consider the flow over a deep cavity at large Reynolds number Re and small Mach number M. The flow can be seen as a system of two coupled elements: the incompressible shear layer (hydrodynamic element), and the compressible volume of fluid inside the cavity (acoustic element). In order to make a first step towards the simple prediction of oscillation amplitudes in aeroacoustic systems, we consider separately the shear layer and the deep cavity. In this study, we treat the cavity as an external element, and we focus specifically on the hydrodynamic response of the shear layer to a prescribed harmonic forcing. This forcing is chosen as a plane wave coming from the cavity end, mimicking the dominant acoustic

resonance mode (quarter-wave mode) at frequency ω_1. We use a triple decomposition and consider the linear harmonic response around the mean flow. In practice, the response to the prescribed forcing is obtained with the linearised Navier–Stokes equations (LNSE) incorporating a turbulence model, while the effect of higher harmonics on the response at ω_1 is neglected. We note that the wavelength of the observed cavity resonance mode is much larger than the shear layer width, such that one can make the compactness assumption, neglect compressibility effects and use incompressible LNSE. For simplicity, the mean flow is taken from nonlinear Navier–Stokes simulations carried out independently with large-eddy simulations (LES) with harmonic forcing at various amplitudes, thus automatically taking into account the effect of higher harmonics on the mean flow. We wish to stress from the start that the mean flow is known *a priori* from LES, and that we do not attempt to predict it. Therefore, our study is fundamentally different from the above-mentioned self-consistent model, although it may be seen as a necessary first step towards its extension to turbulent flows.

Our study addresses several questions: Is it possible to predict accurately the response of the shear layer at different forcing amplitudes using LNSE around the (known) mean flow? Can the saturation mechanism be captured? Can one neglect the effect of higher harmonics on the linear response? None of these questions has obvious *a priori* answers. In the laminar regime, linear stability analysis around mean flows has been shown to produce relevant results in some cases while failing in other cases. For instance, the frequency of limit-cycle oscillations in the flow past a circular cylinder is well predicted by the dominant linear eigenvalue calculated around the mean flow (Barkley 2006). This led Mantič-Lugo, Arratia & Gallaire (2014) to build a self-consistent model for stability analysis in the same vein as that for harmonic response. Turton, Tuckerman & Barkley (2015) observed that linear stability analysis around the mean flow in a laminar thermosolutal convection system reproduces well the nonlinear characteristics of travelling waves; it failed, however, to produce meaningful results for standing waves. It was proposed that the reason might lie in the second harmonic being negligible for travelling waves, and non-negligible for standing waves. This is to be related to the earlier weakly nonlinear analysis of Sipp & Lebedev (2007), who formulated conditions on the second harmonic for the validity of stability analysis around mean flows, and presented a counterexample in a square open cavity. Recently, Meliga (2017) extended the self-consistent model, incorporating the second harmonic. In the turbulent regime, linear stability analysis and linear harmonic response calculations around mean flows are common, in both parallel and global settings (del Álamo & Jiménez 2006; Piot *et al.* 2006; Pujals *et al.* 2009; Hwang & Cossu 2010; Gudmundsson & Colonius 2011; Marquillie, Ehrenstein & Laval 2011; Meliga, Pujals & Serre 2012; Iungo *et al.* 2013; Gikadi, Föller & Sattelmayer 2014; Mettot, Sipp & Bézard 2014; Oberleithner, Schimek & Paschereit 2015; Beneddine *et al.* 2016; Edstrand *et al.* 2016; Tammisola & Juniper 2016). It is not clear, however, if the structure and the amplitude of the response to harmonic forcing are meaningful in general, and if the saturation process can be captured accurately. This is what we assess for the deep cavity of this study.

The paper is organised as follows. The configuration and the mean flow obtained from LES with different forcing amplitudes are presented in § 2. Then, § 3 is devoted to the mean-flow linear response calculated with the LNSE: the problem formulation and numerical method are detailed in §§ 3.1 and 3.2, respectively. Results and comparison with LES results are given in §§ 3.3 and 3.4. Next, the effect of higher harmonics is investigated in § 4, in particular via consideration of optimal forcings

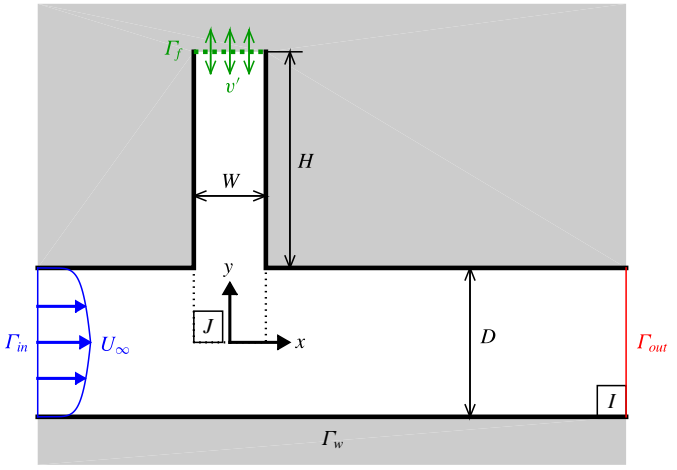

FIGURE 1. (Colour online) Geometry and flow configuration (see main text for dimensions). LNSE calculations are performed in the 2D domain I, around mean flows from LES performed in a 3D domain (same 2D cross-section I, spanwise extension L). The subdomain J is used in measures (3.17) and (3.18) of the response.

(resolvent analysis). Finally, § 5 presents results from a sensitivity analysis that identifies regions where a flow modification or a localised feedback have the largest effect on the optimal harmonic response, which provides useful information for control design. Conclusions are drawn in § 6.

2. Geometry and mean flow

We consider a straight rectangular channel of height $D = 62$ mm, featuring on one side a deep cavity of width $W = 30$ mm and depth $H = 90$ mm (aspect ratio $W/H = 0.33$). Both channel and cavity are of spanwise extension $L = 10$ mm. A two-dimensional (2D) cross-section I is shown in figure 1. The x, y and z directions are denoted streamwise, vertical and spanwise, respectively. With an inlet bulk velocity $U_\infty = 56$ m s^{-1} and a speed of sound $c_0 = 340$ m s^{-1}, the air flow in this channel corresponds to a relatively small Mach number $M = U_\infty/c_0 = 0.16$ and a large Reynolds number $Re = U_\infty W/\nu = 1.5 \times 10^5$.

The effect of an acoustic forcing imposed at the cavity end is investigated by means of three-dimensional (3D) compressible LES. At the inlet Γ_{in} the incoming flow has a turbulent power-law profile of exponent 0.7. Both inlet Γ_{in} and outlet Γ_{out} are acoustically non-reflecting. A no-slip boundary condition is set on the walls Γ_w. At the cavity end Γ_f, a vertical and spatially uniform, time-harmonic forcing $(0,\ v'\cos(\omega_1 t),\ 0)$ is prescribed via a propagative acoustic wave with the NSCBC conditions (Poinsot *et al.* 1992). In this study, the forcing frequency is set to $\omega_1/2\pi = 750$ Hz, close to the frequency of a marginally stable eigenmode and of the largest harmonic response in the unforced flow (see § 3.3). More details about the numerical method will be given in a companion paper by the authors (in preparation). The forcing amplitude v' is varied over more than two orders of magnitude, between 0.025 and 5.0 m s^{-1} (relative velocity v'/U_∞ between 0.045 % and 8.9 %).

The LES mean flow obtained for different forcing amplitudes is shown in figure 2. The streamwise velocity $\overline{U}$ quickly decreases from U_∞ to 0 in the shear layer. A

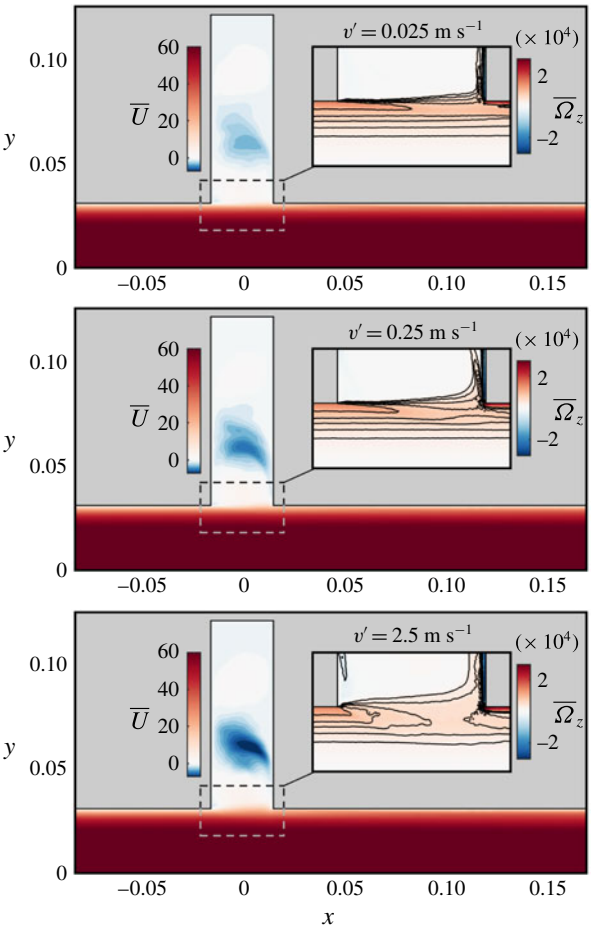

FIGURE 2. (Colour online) Mean streamwise velocity $\overline{U}$ from LES, at forcing amplitudes $v' = 0.025$, 0.25 and 2.5 m s^{-1}. Inset: close-up view of the mean spanwise vorticity $\overline{\Omega}_z = \partial_x \overline{V} - \partial_y \overline{U}$ in the shear layer. Main flow from left to right.

recirculation region is present inside the cavity, and becomes stronger with the forcing amplitude (maximum negative velocity between -3 and -9 m s^{-1}). As shown in the insets, the shear layer thickens and becomes weaker with x, and the mean spanwise vorticity $\overline{\Omega}_z = \partial_x \overline{V} - \partial_y \overline{U}$ clearly diffuses. Larger forcing amplitudes yield a thicker and weaker shear layer.

3. Linear response of the mean flow to harmonic forcing

3.1. *Problem formulation*

3.1.1. *Governing equations for the mean flow and coherent fluctuations*

We start from the Navier–Stokes equations

$$\partial_t \boldsymbol{U} + \boldsymbol{N}(\boldsymbol{U}) = \boldsymbol{F}, \tag{3.1}$$

governing the dynamics of velocity $\boldsymbol{U}(\boldsymbol{x}, t)$ and pressure $P(\boldsymbol{x}, t)$, where

$$\boldsymbol{N}(\boldsymbol{U}) = (\boldsymbol{U}\cdot\boldsymbol{\nabla})\boldsymbol{U} + \frac{1}{\rho}\boldsymbol{\nabla}P - \nu\boldsymbol{\nabla}^2\boldsymbol{U} \tag{3.2}$$

is the nonlinear incompressible Navier–Stokes operator and ρ the fluid density. In this study we restrict our attention to incompressible flows since the Mach number is small, but the spirit of the derivation is similar for compressible flows. Hereafter, we therefore omit the continuity equation $\boldsymbol{\nabla}\cdot\boldsymbol{U} = 0$. The term $\boldsymbol{F}(\boldsymbol{x}, t)$ denotes a space- and time-dependent forcing applied either at a boundary or inside the domain. Following Reynolds & Hussain (1972), the flow is decomposed into its time-averaged component $\overline{\boldsymbol{U}}(\boldsymbol{x})$, coherent fluctuations $\widetilde{\boldsymbol{u}}(\boldsymbol{x}, t)$ and turbulent fluctuations $\boldsymbol{u}'(\boldsymbol{x}, t)$:

$$\boldsymbol{U} = \overline{\boldsymbol{U}} + \widetilde{\boldsymbol{u}} + \boldsymbol{u}'. \tag{3.3}$$

By construction, time averaging ($\overline{\cdot}$) yields the steady mean flow $\overline{\boldsymbol{U}}$ and removes all fluctuations ($\overline{\widetilde{\boldsymbol{u}} + \boldsymbol{u}'} = \boldsymbol{0}$), while phase averaging ($\langle\cdot\rangle$) removes incoherent fluctuations ($\langle\boldsymbol{U}\rangle = \overline{\boldsymbol{U}} + \widetilde{\boldsymbol{u}}$, $\langle\boldsymbol{u}'\rangle = \boldsymbol{0}$). Similar notations are used for other quantities, e.g. pressure, forcing and spanwise vorticity. Substituting this decomposition into (3.1) yields coupled equations for the mean flow and coherent fluctuations:

$$\boldsymbol{N}(\overline{\boldsymbol{U}}) = -\boldsymbol{\nabla}\cdot(\overline{\widetilde{\boldsymbol{u}}\widetilde{\boldsymbol{u}}} + \overline{\boldsymbol{u}'\boldsymbol{u}'}) + \overline{\boldsymbol{F}}, \tag{3.4a}$$

$$\partial_t\widetilde{\boldsymbol{u}} + \boldsymbol{L}(\overline{\boldsymbol{U}})\widetilde{\boldsymbol{u}} = -\boldsymbol{\nabla}\cdot(\widetilde{\widetilde{\boldsymbol{u}}\widetilde{\boldsymbol{u}}} + \widetilde{\boldsymbol{u}'\boldsymbol{u}'}) + \widetilde{\boldsymbol{f}}, \tag{3.4b}$$

where $\boldsymbol{L}(\overline{\boldsymbol{U}})$ is the Navier–Stokes operator linearised around the mean flow,

$$\boldsymbol{L}(\overline{\boldsymbol{U}})\widetilde{\boldsymbol{u}} = (\overline{\boldsymbol{U}}\cdot\boldsymbol{\nabla})\widetilde{\boldsymbol{u}} + (\widetilde{\boldsymbol{u}}\cdot\boldsymbol{\nabla})\overline{\boldsymbol{U}} + \frac{1}{\rho}\boldsymbol{\nabla}\widetilde{p} - \nu\boldsymbol{\nabla}^2\widetilde{\boldsymbol{u}}. \tag{3.5}$$

Equation (3.4) shows that, due to the forcing from the coherent and turbulent Reynolds stresses $\widetilde{\boldsymbol{u}}\widetilde{\boldsymbol{u}} + \boldsymbol{u}'\boldsymbol{u}'$, the mean flow $\overline{\boldsymbol{U}}$ differs from the steady base flow $\boldsymbol{U}_b$, which is a solution of the stationary Navier–Stokes equations $\boldsymbol{N}(\boldsymbol{U}_b) = \overline{\boldsymbol{F}}$.

Focusing on a coherent time-harmonic forcing at frequency ω_1,

$$\overline{\boldsymbol{F}} = \boldsymbol{0}, \quad \widetilde{\boldsymbol{f}}(\boldsymbol{x}, t) = \widetilde{\boldsymbol{f}}_1(\boldsymbol{x})\mathrm{e}^{\mathrm{i}\omega_1 t} + \text{c.c.}, \quad \boldsymbol{f}' = \boldsymbol{0}, \tag{3.6a–c}$$

where c.c. stands for complex conjugate, the coherent response is assumed to fluctuate at the forcing frequency and higher harmonics:

$$\widetilde{\boldsymbol{u}}(\boldsymbol{x}, t) = \sum_{n\neq 0}\widetilde{\boldsymbol{u}}_n(\boldsymbol{x})\mathrm{e}^{\mathrm{i}n\omega_1 t} = \sum_{n>0}\widetilde{\boldsymbol{u}}_n(\boldsymbol{x})\mathrm{e}^{\mathrm{i}n\omega_1 t} + \text{c.c.} \quad (\widetilde{\boldsymbol{u}}_{-n} = \widetilde{\boldsymbol{u}}_n^*). \tag{3.7}$$

Introducing this Fourier decomposition into (3.4) yields an infinite system of equations for the mean flow $\overline{\boldsymbol{U}}$ and each coherent fluctuation $\widetilde{\boldsymbol{u}}_n$:

$$\boldsymbol{N}(\overline{\boldsymbol{U}}) = -\sum_{n\neq 0}\boldsymbol{\nabla}\cdot\widetilde{\boldsymbol{u}}_n\widetilde{\boldsymbol{u}}_{-n} - \boldsymbol{\nabla}\cdot\overline{\boldsymbol{u}'\boldsymbol{u}'}, \tag{3.8a}$$

$$\mathrm{i}n\omega_1\widetilde{\boldsymbol{u}}_n + \boldsymbol{L}(\overline{\boldsymbol{U}})\widetilde{\boldsymbol{u}}_n = -\sum_{m\neq n,0}\boldsymbol{\nabla}\cdot\widetilde{\boldsymbol{u}}_m\widetilde{\boldsymbol{u}}_{n-m} - \boldsymbol{\nabla}\cdot(\widetilde{\boldsymbol{u}'\boldsymbol{u}'})_n + \delta_{n1}\widetilde{\boldsymbol{f}}_1, \tag{3.8b}$$

where $\widetilde{(\boldsymbol{u}'\boldsymbol{u}')}_n$ denotes the coherent component at frequency $n\omega_1$ of the turbulent Reynolds stresses, and δ_{n1} is the Kronecker delta (equal to 1 if $n = 1$, and to 0 otherwise). For instance, the mean flow and first two harmonics are governed by

$$\boldsymbol{N}(\overline{\boldsymbol{U}}) = -(\widetilde{\boldsymbol{\psi}}_{1,-1} + \widetilde{\boldsymbol{\psi}}_{2,-2} + \cdots) - \boldsymbol{\nabla}\cdot\overline{\boldsymbol{u}'\boldsymbol{u}'}, \tag{3.9a}$$

$$(\mathrm{i}\omega_1 + \boldsymbol{L}(\overline{\boldsymbol{U}}))\widetilde{\boldsymbol{u}}_1 = -(\widetilde{\boldsymbol{\psi}}_{2,-1} + \widetilde{\boldsymbol{\psi}}_{3,-2} + \cdots) - \boldsymbol{\nabla}\cdot\widetilde{(\boldsymbol{u}'\boldsymbol{u}')}_1 + \widetilde{\boldsymbol{f}}_1, \tag{3.9b}$$

$$(2\mathrm{i}\omega_1 + \boldsymbol{L}(\overline{\boldsymbol{U}}))\widetilde{\boldsymbol{u}}_2 = -(\widetilde{\boldsymbol{\psi}}_{1,1} + \widetilde{\boldsymbol{\psi}}_{3,-1} + \cdots) - \boldsymbol{\nabla}\cdot\widetilde{(\boldsymbol{u}'\boldsymbol{u}')}_2, \tag{3.9c}$$

where we have introduced the notation

$$\widetilde{\boldsymbol{\psi}}_{j,k} = \boldsymbol{\nabla}\cdot\widetilde{\boldsymbol{u}}_j\widetilde{\boldsymbol{u}}_k + \text{c.c.} \quad \text{if } j \neq k, \qquad \widetilde{\boldsymbol{\psi}}_{j,j} = \boldsymbol{\nabla}\cdot\widetilde{\boldsymbol{u}}_j\widetilde{\boldsymbol{u}}_j, \tag{3.10a,b}$$

for the divergence of the coherent Reynolds stresses. At this stage no assumption has been made, other than the response fluctuates at ω_1 and higher harmonics; the model is therefore general except for flows exhibiting other frequencies (for instance, subharmonics that appear via vortex pairing in some jets and mixing layers).

3.1.2. *Turbulent viscosity*

The effect of the unknown turbulent Reynolds stresses $\boldsymbol{u}'\boldsymbol{u}'$ on coherent fluctuations in (3.8) is accounted for with a turbulence model that relates $\widetilde{\boldsymbol{u}'\boldsymbol{u}'}$ to $\widetilde{\boldsymbol{u}}$ via a turbulent viscosity ν_t, such that (3.9) becomes

$$(\mathrm{i}\omega_1 + \boldsymbol{L}(\overline{\boldsymbol{U}}))\widetilde{\boldsymbol{u}}_1 = -(\widetilde{\boldsymbol{\psi}}_{2,-1} + \widetilde{\boldsymbol{\psi}}_{3,-2} + \cdots) + \widetilde{\boldsymbol{f}}_1, \tag{3.11}$$

where $\boldsymbol{L}$ now contains the modified viscosity $\nu + \nu_t$. Specifically, we use a classical eddy viscosity model. The unknown coherent component of the turbulent Reynolds stresses $\widetilde{\boldsymbol{u}'\boldsymbol{u}'}$ is assumed to be proportional to the coherent strain rate $\widetilde{\boldsymbol{S}} = (\boldsymbol{\nabla}\widetilde{\boldsymbol{u}} + \boldsymbol{\nabla}\widetilde{\boldsymbol{u}}^{\mathrm{T}})/2$ (Boussinesq approximation):

$$\widetilde{\boldsymbol{u}'\boldsymbol{u}'} - \tfrac{2}{3}\widetilde{q}\boldsymbol{I} = -2\nu_t\widetilde{\boldsymbol{S}}, \tag{3.12}$$

where $\widetilde{q} = \widetilde{\boldsymbol{u}'\cdot\boldsymbol{u}'}/2$ is the kinetic energy and $\boldsymbol{I}$ the identity tensor. In this study the turbulent viscosity ν_t is taken as space-dependent, and calculated at each location according to

$$\nu_t(\boldsymbol{x}) = -\frac{\overline{\boldsymbol{u}'\boldsymbol{u}'} : \overline{\boldsymbol{S}}}{2\overline{\boldsymbol{S}} : \overline{\boldsymbol{S}}}, \tag{3.13}$$

where $:$ denotes the Frobenius inner product. In other words, at each location ν_t can be seen as resulting from the least-squares minimisation of the overdetermined system of equations $\overline{\boldsymbol{u}'\boldsymbol{u}'} = -2\nu_t\overline{\boldsymbol{S}}$.

As explained in Pope (2000), the above model is a twofold simplification: first, it assumes that turbulent quantities ($\widetilde{\boldsymbol{u}'\boldsymbol{u}'}$) can be related to the coherent motion ($\widetilde{\boldsymbol{S}}$); second, it assumes that this constitutive relation is specifically of the form (3.12), i.e. linear isotropic (directly analogous to the relation for the viscous stress in a Newtonian fluid). Although the turbulent viscosity hypothesis is incorrect in general, it has been found reasonable in many simple turbulent shear flows (round jet, mixing layer, channel flow, boundary layer) where the turbulent and coherent characteristics change relatively slowly, following the mean flow.

In (3.13) we have implicitly assumed that coherent fluctuations do not affect the turbulent viscosity, i.e. although it is possible to linearise the turbulent model itself

(Meliga *et al.* 2012; Mettot *et al.* 2014; Viola *et al.* 2014), here we use a turbulence viscosity computed once and for all for each given mean flow.

The steady component of the turbulent Reynolds stresses $\overline{\boldsymbol{u}'\boldsymbol{u}'}$ and the mean strain rate $\overline{\boldsymbol{S}} = (\boldsymbol{\nabla}\overline{\boldsymbol{U}} + \boldsymbol{\nabla}\overline{\boldsymbol{U}}^{\mathrm{T}})/2$ are evaluated from the LES. It should be noted that $\overline{\boldsymbol{S}}$ is a direct output of the LES, whereas the calculation of $\overline{\boldsymbol{u}'\boldsymbol{u}'}$ requires further processing: indeed, the statistics of the total LES velocity field contain the steady component of both turbulent and coherent Reynolds stresses $\overline{\boldsymbol{u}'\boldsymbol{u}'} + \overline{\widetilde{\boldsymbol{u}}\widetilde{\boldsymbol{u}}}$. This can be overlooked if the stresses $\overline{\widetilde{\boldsymbol{u}}\widetilde{\boldsymbol{u}}}$ are small compared to $\overline{\boldsymbol{u}'\boldsymbol{u}'}$ (Kitsios *et al.* 2010; Viola *et al.* 2014), which is not the case here because substantial coherent fluctuations are produced by the harmonic forcing in the large-amplitude regime. Therefore, before computing the turbulent viscosity, we first remove the coherent contribution $\overline{\widetilde{\boldsymbol{u}}_1\widetilde{\boldsymbol{u}}_{-1}}$ at the fundamental frequency, with $\widetilde{\boldsymbol{u}}_{\pm 1}$ obtained from frequency analysis. Specifically, coherent fluctuations $\widetilde{\boldsymbol{u}}_1$ from the 3D LES are computed by extracting 2D time-dependent velocity fields in the mid-plane $z = 0$, and performing a Fourier transform at the frequency of interest ω_1. Some authors have used an alternative approach based on energetic structures obtained from proper orthogonal decomposition (Tammisola & Juniper 2016) or have proposed weighting the turbulent viscosity by a laminar–turbulent intermittency factor (Oberleithner, Paschereit & Wygnanski 2014).

3.1.3. *Simplified model*

In this paper, we wish to assess the possibility to capture correctly the amplification and saturation using a simplified model. We will compute coherent fluctuations at the frequency of interest ω_1 via the linear response problem

$$(\mathrm{i}\omega_1 + \boldsymbol{L}(\overline{\boldsymbol{U}}))\widetilde{\boldsymbol{u}}_1 = \widetilde{\boldsymbol{f}}_1. \tag{3.14}$$

In other words, we neglect nonlinear forcing terms $\widetilde{\boldsymbol{\psi}}_{j,1-j}$ arising from the interaction of coherent higher harmonics (even though those higher harmonics themselves, $\widetilde{\boldsymbol{u}}_n$, $|n| \geqslant 2$, may not be negligible), while we retain nonlinearities contained in the LES mean flow as well as nonlinearities involved in the turbulent viscosity. Put simply, we study the linearised dynamics of coherent fluctuations around (known) mean flows, with a turbulent viscosity model.

3.2. *Numerical method*

The 2D linear response to time-harmonic forcing is calculated around the mean flow obtained from LES (§ 2). The LNSE (3.14) are recast in variational form and discretised in domain I with the finite-element software FreeFem++ (Hecht 2012), using P2 and P1 Taylor–Hood elements for velocity and pressure, respectively (Boujo, Ehrenstein & Gallaire 2013; Boujo & Gallaire 2015). The 2D mesh contains approximately 330 000 triangular elements, strongly clustered in the mixing layer (see appendix A for a convergence study assessing the influence of the mesh size). Boundary conditions are as follows: $\widetilde{\boldsymbol{u}}_1 = \boldsymbol{0}$ at the inlet Γ_{in} and on the walls Γ_w, stress-free condition $(1/\rho)\widetilde{p}_1\boldsymbol{n} + 2(\nu + \nu_t)\widetilde{\boldsymbol{S}}_1 \cdot \boldsymbol{n} = 0$ at the outlet Γ_{out}, and spatially uniform vertical forcing $\widetilde{\boldsymbol{u}}_1 = v'\boldsymbol{e}_y$ at the cavity end Γ_f.

3.3. *Unforced case: linear stability analysis and linear harmonic response*

We first focus on the unforced case, $v' = 0$. Before moving on to the harmonic response problem, we investigate linear stability by solving the eigenvalue problem

$$(\sigma + \mathrm{i}\omega)\widetilde{\boldsymbol{u}} + \boldsymbol{L}(\overline{\boldsymbol{U}})\widetilde{\boldsymbol{u}} = \boldsymbol{0} \tag{3.15}$$

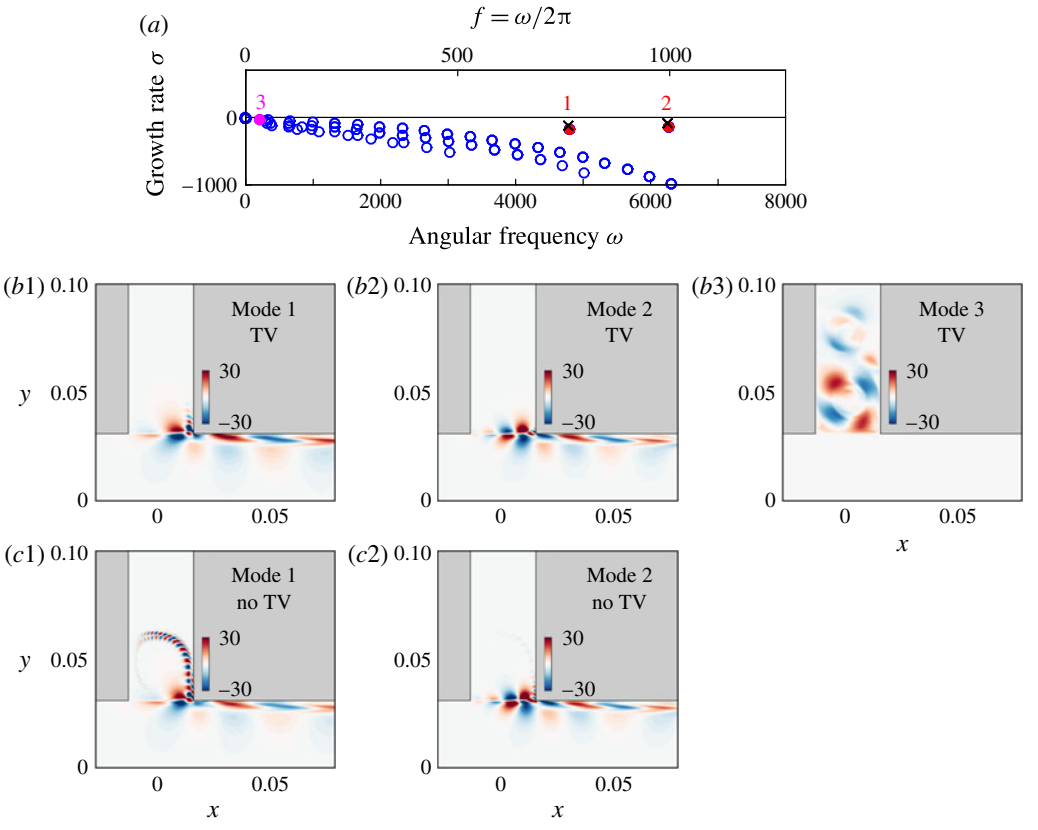

FIGURE 3. (Colour online) Global linear stability around the unforced mean flow ($v' = 0$). (*a*) Eigenvalues lie on continuous branches, except marginally stable eigenvalues 1 and 2, which stand out at $\omega/2\pi = 750$ and 1000 Hz. These two eigenvalues are not substantially affected by discarding turbulent viscosity (crosses). (*b*,*c*) Eigenmodes (unit norm; streamwise component, real part). Modes 1 and 2 are located in the shear layer and the downstream boundary layer, computed either with turbulent viscosity ('TV', panels $b1, b2$) or without ('no TV', panels $c1, c2$). ($b3$) Other modes are located inside the cavity.

for infinitesimal perturbations $\widetilde{\boldsymbol{u}}$ around the LES mean flow $\overline{\boldsymbol{U}}$, with the numerical method as described in § 3.2. As shown in the spectrum in figure 3(*a*), all eigenmodes are stable (growth rate $\sigma \leqslant 0$). Most eigenvalues fall on continuous branches, and are more stable at larger frequencies. Two eigenmodes (denoted 1 and 2) stand out, however, at frequencies close to 750 and 1000 Hz, and are marginally stable (small growth rate compared to the angular frequency, $|\sigma| \ll \omega$). Marginal stability in mean flows has been observed in some laminar and turbulent flows, as well as counterexamples (Barkley 2006; Sipp & Lebedev 2007; Turton *et al.* 2015; Meliga 2017). Here, modes 1 and 2 are located primarily around the downstream corner, as shown in figure 3($b1$,$b2$). They are associated with spatio-temporal growth along the shear layer via the Kelvin–Helmholtz instability, decay in the downstream boundary layer, and feed back via a pressure wave from the downstream corner back to the upstream corner, reminiscent of leading eigenmodes observed in other cavities (Åkervik *et al.* 2007; Sipp & Lebedev 2007; Barbagallo, Sipp & Schmid 2009).

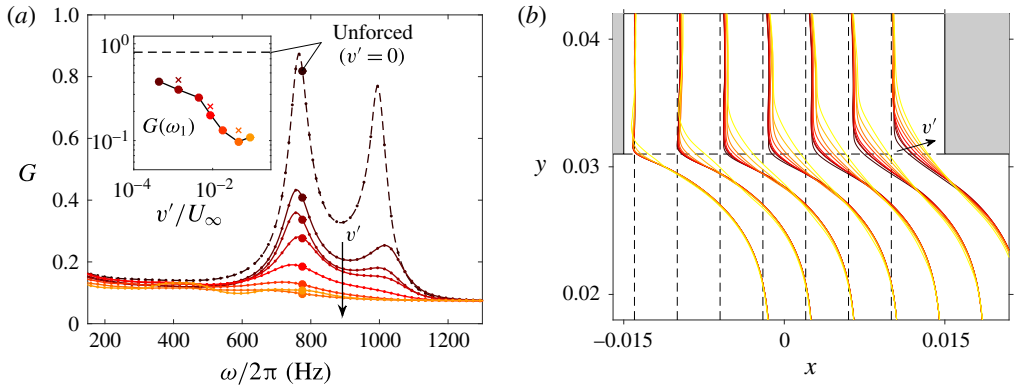

FIGURE 4. (Colour online) (*a*) Linear harmonic gain $G(\omega)$ of the turbulent mean flow forced at $\omega_1/2\pi = 750$ Hz at different amplitudes v'. Inset: $G(\omega_1)$ in logarithmic scale (and a few results without turbulent viscosity shown as crosses). (*b*) Profiles of mean streamwise velocity $\overline{U}$.

Modes 1 and 2 exhibit approximately one and two wavelengths across the cavity, respectively, i.e. smaller structures correspond to higher frequencies. Other modes are located inside the cavity, e.g. mode 3 in figure 3(*b*3). Discarding turbulent viscosity in the linear stability analysis (i.e. in $\boldsymbol{L}$ in the eigenvalue problem (3.15)) does not affect substantially eigenvalues 1 and 2 (black crosses in figure 3*a*), and has a limited impact on the structure of modes 1 and 2 in the shear layer (figure 3*c*1, *c*2).

Next, the linear response of the mean unforced flow to harmonic forcing on Γ_f is characterised in terms of kinetic energy in domain I with the gain

$$G(\omega) = \frac{1}{v'} \left(\iint_I |\widetilde{\boldsymbol{u}}_1|^2 \, \mathrm{d}\boldsymbol{x} \right)^{1/2}. \tag{3.16}$$

Figure 4(*a*) shows the gain obtained from the LNSE over a broad range of forcing frequencies (dashed line). The forcing is amplified preferentially in the frequency range 600–1200 Hz, with clear peaks close to 750 and 1000 Hz that can be related to the marginally stable modes 1 and 2.

3.4. *Forced cases, saturation of the linear harmonic response*

We now turn our attention to mean flows obtained from LES with harmonic forcing at $\omega_1/2\pi = 750$ Hz, and recompute the linear response to harmonic forcing. In these mean flows, the gain consistently decreases with the forcing amplitude (solid lines in figure 4*a*).

In the following, we focus on the linear response to harmonic forcing at the frequency ω_1 of the dominant peak. At this specific frequency (inset), the gain decreases by approximately one order of magnitude from the unforced regime to the large-amplitude forcing regime $v' \gtrsim 2.5$ m s^{-1}. It should be noted that this effect comes entirely from the mean flow, which varies with v'. Specifically, the mixing layer becomes thicker as v' increases (figure 4*b*), suggesting that the weaker shear is the main cause for the reduced amplification. The gain $G(\omega_1)$ is slightly lower with turbulent viscosity (dots) than without (crosses), consistent with the limited stabilising influence of turbulent viscosity on the marginally stable eigenmode 1 (figure 3*a*).

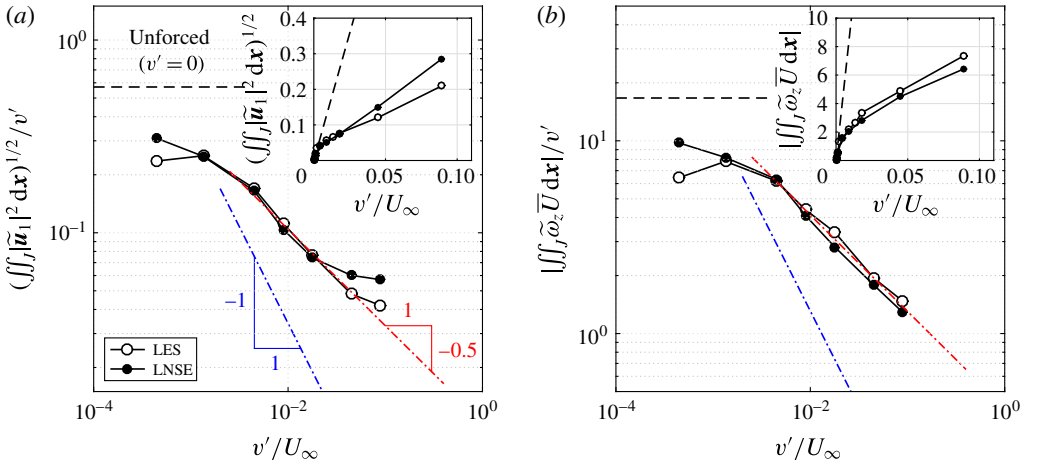

FIGURE 5. (Colour online) Harmonic gain (logarithmic scale) at $\omega_1/2\pi = 750$ Hz versus forcing amplitude, from LES (open symbols) and LNSE (filled symbols). The gain is calculated with the response measured in terms of (*a*) kinetic energy (3.17) and (*b*) dominant contribution of the vertical component of the unsteady Coriolis force (3.18). The linear gain for the unforced flow ($v'=0$) is shown as a horizontal dashed line. Also shown are the slope -0.5 (red) that fits the data for $v'/U_\infty \geqslant 0.45\,\%$, and the slope -1 (blue) that would be obtained for full saturation. Insets: harmonic response (linear scale).

Next, we take a closer look at the rectangular subdomain $J = \{(x, y) \mid -W/2 \leqslant x \leqslant W/2, 0 \leqslant y\}$ spanning exactly the streamwise extension of the cavity. Figure 5(*a*) compares the harmonic gain restricted to region J, obtained from LNSE (linear response) and LES (Fourier transform mentioned in § 3.1) at ω_1:

$$\frac{1}{v'}\left(\iint_J |\widetilde{\boldsymbol{u}}_1|^2 \,\mathrm{d}\boldsymbol{x}\right)^{1/2}. \tag{3.17}$$

The overall agreement is very good, with LNSE capturing well the decrease in gain observed in the LES. The slight discrepancy at very low forcing amplitude ($v' = 0.025$ m s^{-1}) can be ascribed to the small signal-to-noise ratio in the LES, which makes it difficult to measure the gain accurately. In the large-amplitude forcing regime, LNSE overestimates the coherent response, which points to non-negligible contributions from higher harmonics and/or to a deteriorating turbulent viscosity model. The inset illustrates the saturation of the response itself (prior to normalisation by v'), with the slope quickly departing from the LNSE result obtained with the unforced flow (dashed line).

Figure 5(*b*) shows an alternative measure of the gain, useful in an aeroacoustic context: we define

$$\frac{1}{v'}\left|\iint_J \widetilde{\omega}_z\,\overline{U}\,\mathrm{d}\boldsymbol{x}\right|, \tag{3.18}$$

where $\widetilde{\omega}_z = \partial_x\widetilde{v} - \partial_y\widetilde{u}$ is the spanwise vorticity of the coherent response. This measure gives insight into vortex sound production, since the Coriolis force $\boldsymbol{\Omega}\times\boldsymbol{U}$ is related to the acoustic power $\mathcal{P}$ of a low-Mach-number compact vorticity distribution, as expressed for instance by Howe's formula (Howe 1980)

$$\mathcal{P} = -\iint \overline{\rho}(\boldsymbol{\Omega}\times\boldsymbol{U})\cdot\boldsymbol{u}_{ac}\,\mathrm{d}\boldsymbol{x}, \tag{3.19}$$

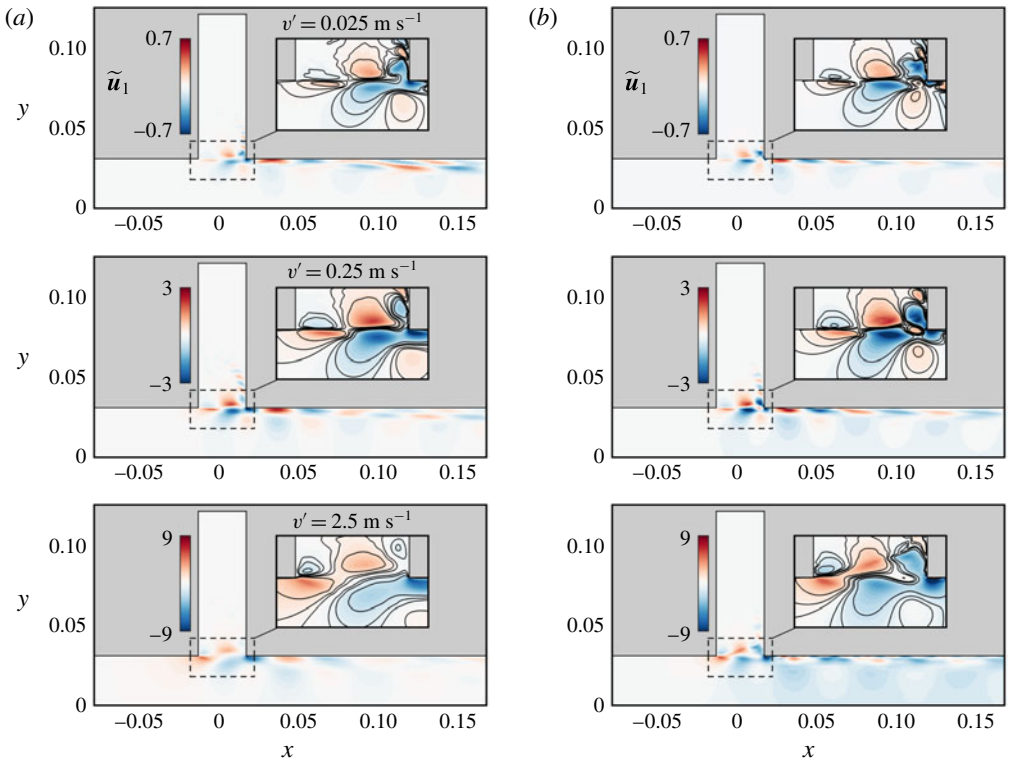

FIGURE 6. (Colour online) Streamwise component of $\widetilde{\boldsymbol{u}}_1$ at ω_1. (*a*) LES spectral component. (*b*) LNSE linear harmonic response around the mean flow. Forcing amplitudes $v' = 0.025,\ 0.25$ and 2.5 m s^{-1}.

where $\boldsymbol{U}$ is the total unsteady velocity field, $\boldsymbol{\Omega}$ the total vorticity field, and $\boldsymbol{u}_{ac}$ the acoustic (irrotational) component of the fluctuation. In the present configuration, the above expression is well approximated by the contributions from the vertical component v_{ac} of the acoustic fluctuations and from the vertical component $\Omega_z U$ of the Coriolis force. In addition, the dominant contribution to the time-averaged power comes from $\widetilde{\omega}_z \overline{U}$, hence our choice for (3.18) (see a companion paper by the authors (in preparation) for an in-depth analysis and discussion). Here again, the agreement between LES and LNSE results is very good, which suggests that the linearised approach can provide useful quantitative estimates of the produced acoustic power.

Both gains (3.17) and (3.18) decrease like $\sim 1/\sqrt{v'}$, as shown by the red line of slope -0.5. This is weaker than full saturation, which would yield $\sim 1/v'$ (blue line of slope -1), i.e. a response not increasing at all when the forcing amplitude increases. Graf & Ziada (2010) and Nakiboğlu, Manders & Hirschberg (2012) reported a similar saturation slope of approximately -0.6 in other cavity flows (deep circular cavity $W/H = 0.08$ and shallow axisymmetric cavity $W/H = 1.48$, respectively).

The spatial structure of the harmonic response at ω_1 is shown in figure 6, obtained from the LNSE calculation and from the Fourier decomposition (§ 3.1) of LES data. The response is localised in the mixing layer, and in the downstream boundary layer. At low and medium forcing amplitudes, it has a distinct wave packet structure and experiences a clear streamwise growth, with weak perturbations generated close to the

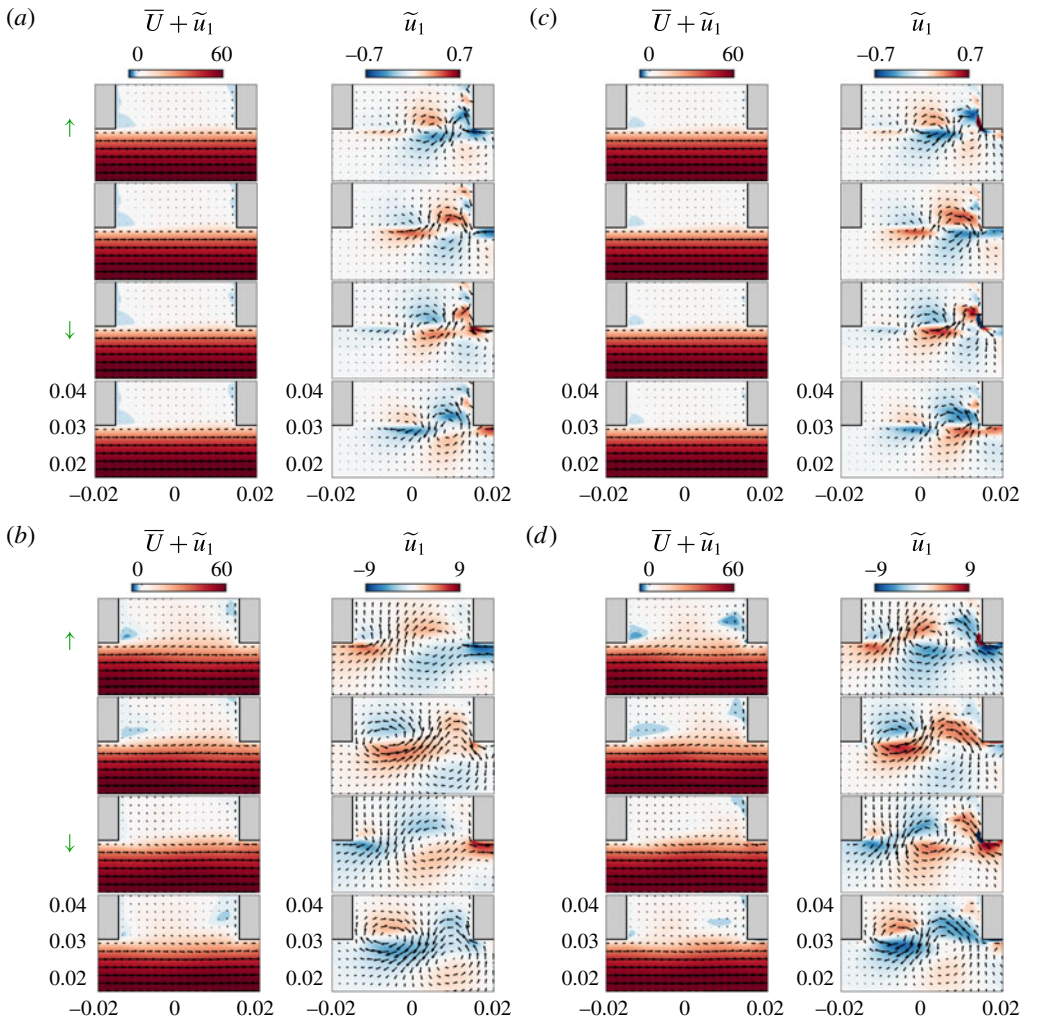

FIGURE 7. (Colour online) Contours of streamwise velocity: phase-averaged velocity $\overline{U}+\widetilde{u}_1$ and coherent velocity fluctuations $\widetilde{u}_1$. Overlaid are arrows of the phase-averaged and coherent fluctuating velocity fields $\overline{\boldsymbol{U}}+\widetilde{\boldsymbol{u}}_1$ and $\widetilde{\boldsymbol{u}}_1$, respectively. (*a*,*b*) LES, (*c*,*d*) LNSE. Forcing amplitudes: (*a*,*c*) $v'=0.025$ m s^{-1}, (*b*,*d*) $v'=2.5$ m s^{-1}. Time instants in each panel, from top to bottom: t (forcing directed upwards ↑), $t+T_1/4$, $t+T_1/2$ (forcing directed downwards ↓) and $t+3T_1/4$.

upstream corner and amplified while convected by the mean flow to the downstream corner. This is typical of the linear response or instability of mixing layers. At larger forcing amplitudes, the wave packet structure is less well organised and perturbations are convected with no substantial growth. At this frequency, one wavelength of the coherent response (i.e. one vortical structure) almost exactly fills the cavity width. The shape and amplitude of the responses obtained from LNSE and LES are very similar, except in the vicinity of the downstream corner and for the largest forcing amplitudes.

Figures 7 and 8 show snapshots of the response obtained from LES and LNSE at four time instants of an oscillation cycle separated by $T_1/4$, with $T_1=2\pi/\omega_1$

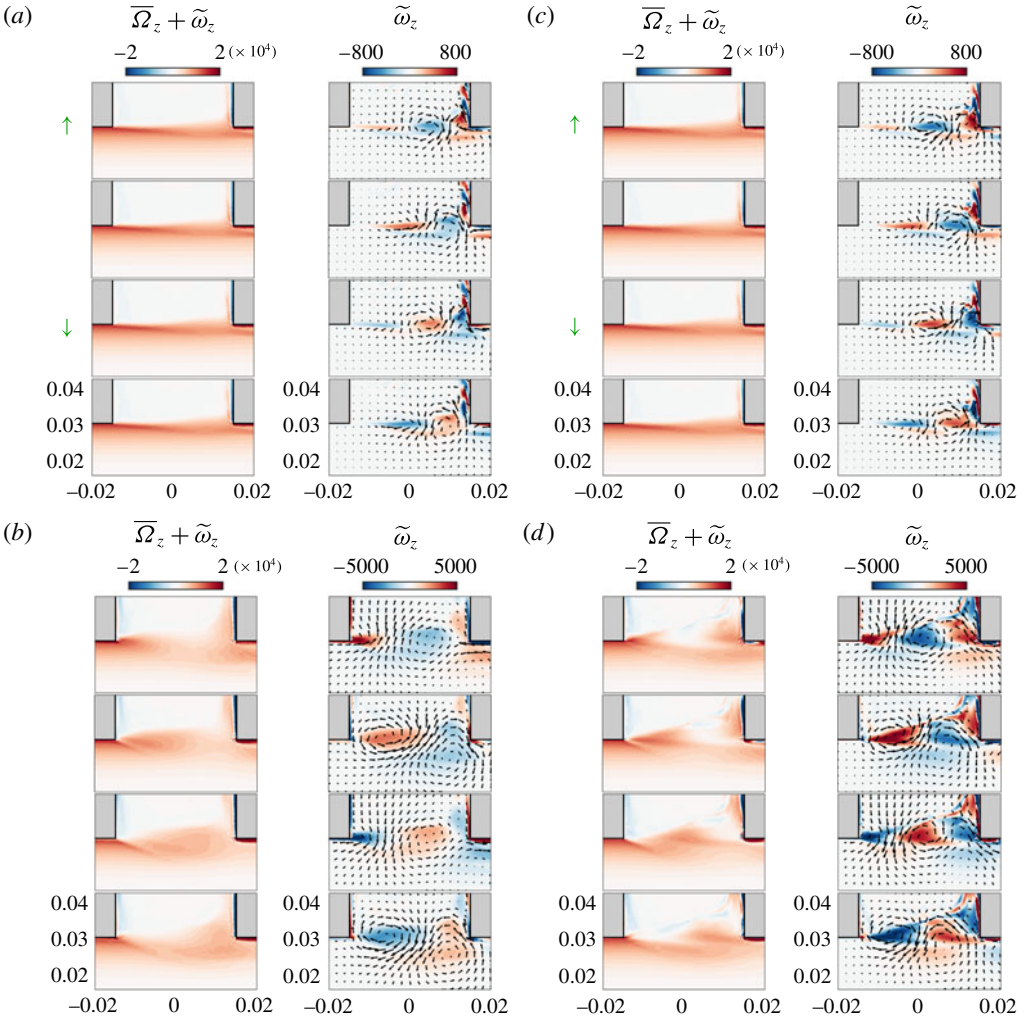

FIGURE 8. (Colour online) Contours of spanwise vorticity: phase-averaged vorticity $\overline{\Omega}_z + \widetilde{\omega}_z$ and coherent vorticity fluctuations $\widetilde{\omega}_z$. Overlaid are arrows of the coherent fluctuating velocity field $\widetilde{\boldsymbol{u}}_1$. (*a*,*b*) LES, (*c*,*d*) LNSE. Forcing amplitudes: (*a*,*c*) $v' = 0.025$ m s^{-1}, (*b*,*d*) $v' = 2.5$ m s^{-1}. Time instants in each panel, from top to bottom: t (forcing directed upwards ↑), $t + T_1/4$, $t + T_1/2$ (forcing directed downwards ↓) and $t + 3T_1/4$.

the forcing period. At small forcing amplitude (figures 7*a*,*c* and 8*a*,*c*), the gain is larger than at other forcing amplitudes but the resulting coherent response is small compared to the mean flow, and oscillations in the total flow are barely distinguishable. Snapshots of streamwise velocity and spanwise vorticity depict the formation and advection of two main vortical structures of opposite vorticity in the first and second half-periods. At larger forcing amplitude (figures 7*b*,*d* and 8*b*,*d*), the amplification is substantially smaller but the coherent response is large enough that fluctuations in the total flow are visible. One can clearly observe the role of the upstream corner in the formation of vortical structures, with $\omega_z > 0$ when the forcing is directed upwards (towards the cavity end) and, $T_1/2$ later, $\omega_z < 0$ when the forcing is directed downwards (towards the main channel).

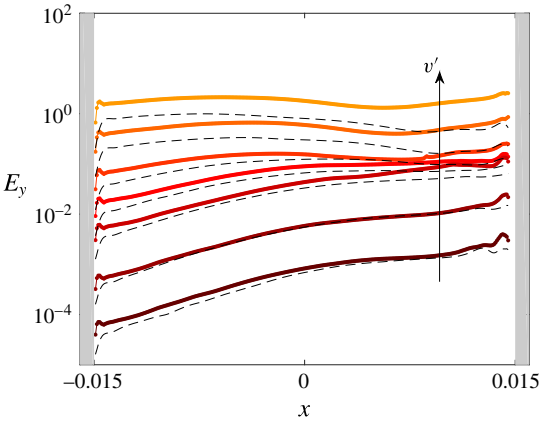

FIGURE 9. (Colour online) Streamwise evolution of the energy density (3.20). Thick solid lines, LNSE harmonic response; thin dashed lines, LES spectral component.

As observed in figures 6 and 7, the location of strongest response, where $\widetilde{\boldsymbol{u}}_1$ is maximal, moves upstream as the forcing amplitude $|v'|$ increases. This is further quantified in figure 9, which represents the streamwise evolution of the coherent kinetic energy integrated vertically in J ($y > 0$), i.e. the coherent energy density

$$E_y(x) = \int_{y>0} E(x, y)\,\mathrm{d}y = \frac{1}{2}\int_{y>0} |\widetilde{u}_1|^2 + |\widetilde{v}_1|^2\,\mathrm{d}y. \tag{3.20}$$

At low forcing amplitudes, E_y increases exponentially with x, consistent with the streamwise amplification mentioned earlier and with a linear amplification scenario, and reaches its maximum close to the downstream corner. As the forcing amplitude increases, the region of exponential amplification becomes shorter and eventually vanishes; consequently, E_y reaches its maximum already near the middle of the cavity, and eventually even in the first half.

This upstream migration can be understood in terms of the mean flow distortion induced by the Reynolds stresses. As mentioned in § 3, the mean flow is forced by Reynolds stress divergence terms (see e.g. (3.4)). As the forcing amplitude increases, coherent Reynolds stresses build up earlier upstream (figure 10), leading to a thickening of the mean shear layer. In turn, the coherent response building up around this increasingly diffused mean flow benefit from a reduced potential for amplification, and saturate earlier upstream. This segregated yet coupled description, i.e. the interaction between (i) the nonlinear mean flow forced by the coherent response and (ii) the linear monochromatic coherent response around the mean flow, is the central ingredient of the simplified self-consistent model proposed to predict the saturation mechanism at play under harmonic forcing (Mantič-Lugo & Gallaire 2016).

4. Validity of the monochromatic approximation

4.1. *Amplitude of higher harmonics and corresponding forcing terms*

In the previous section we have considered the linear response at only one frequency, equal to the forcing frequency ω_1, and we have focused on the external forcing $\widetilde{\boldsymbol{f}}_1$,

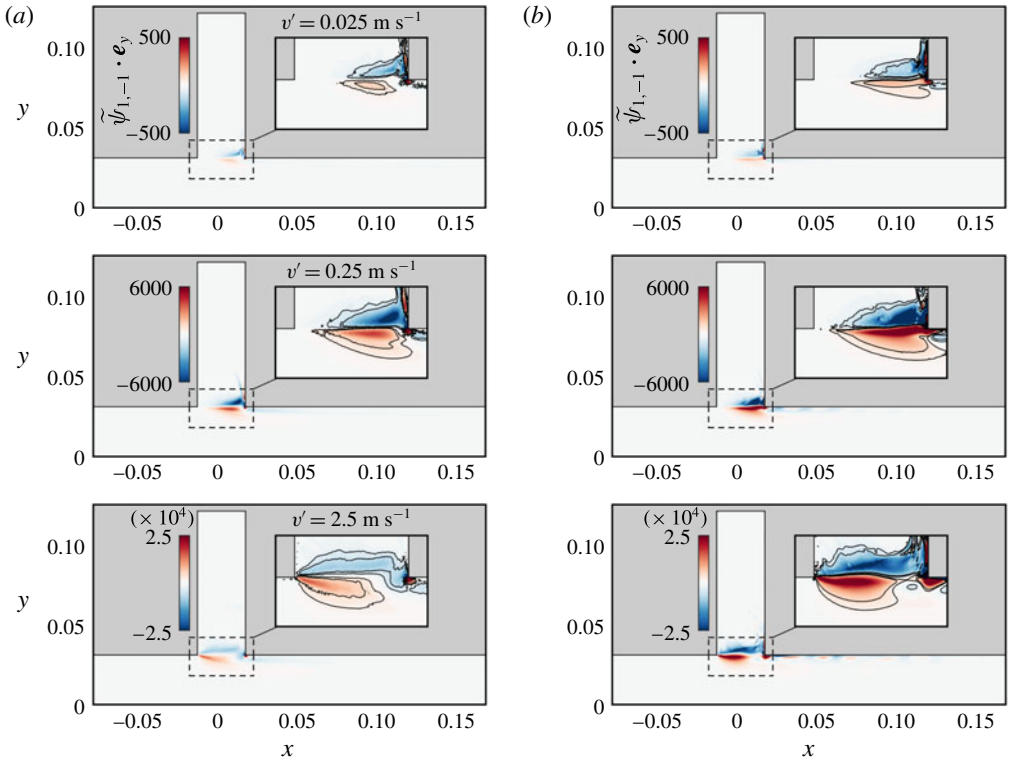

FIGURE 10. (Colour online) Divergence of the coherent Reynolds stress, $\widetilde{\boldsymbol{\psi}}_{1,-1}$ (vertical component), acting as a forcing term for the mean flow (see (3.9)). (*a*) LES. (*b*) LNSE. Forcing at ω_1, amplitudes $v' = 0.025$, 0.25 and 2.5 m s^{-1}.

neglecting other forcing terms arising at ω_1 from the interaction of higher-frequency coherent fluctuations, i.e. Reynolds stress divergence terms $\widetilde{\boldsymbol{\psi}}_{j,1-j}$, $j \geqslant 2$, in (3.11). The good agreement found between the response obtained in this LNSE framework and the flow computed with a fully nonlinear LES suggests that the nonlinear interaction of higher harmonics plays a negligible role on the response. (Note that this still requires the correct mean flow $\overline{\boldsymbol{U}}$, which is crucially determined by $\widetilde{\boldsymbol{\psi}}_{1,-1}$ and possibly influenced by higher-order terms $\widetilde{\boldsymbol{\psi}}_{j,-j}$ as well. Here we use the fully nonlinear LES mean flow; a predictive method doing without direct nonlinear simulations would have to account for these Reynolds stresses carefully.) In the following, we investigate this aspect further.

In general, if higher harmonics are small, their interaction is necessarily small too. We note that, in the present flow, the second harmonic $\widetilde{\boldsymbol{u}}_2$ (extracted from the LES at $\omega_2 = 2\omega_1$) is smaller than $\widetilde{\boldsymbol{u}}_1$ but far from negligible: the ratio of L^2 norms $\|\widetilde{\boldsymbol{u}}_1\|/\|\widetilde{\boldsymbol{u}}_2\|$ is less than one order of magnitude (figure 11*a*). In Turton *et al.* (2015), linear stability analysis around the mean flow in a laminar thermosolutal convection system reproduced well nonlinear characteristics for travelling waves whereas it failed for standing waves, which was explained by a negligible (respectively, non-negligible) second harmonic in the former (respectively, latter) case.

Higher harmonics, albeit not negligible, may still contribute only marginally to the harmonic response at ω_1, either (i) if their interaction as Reynolds stress divergence

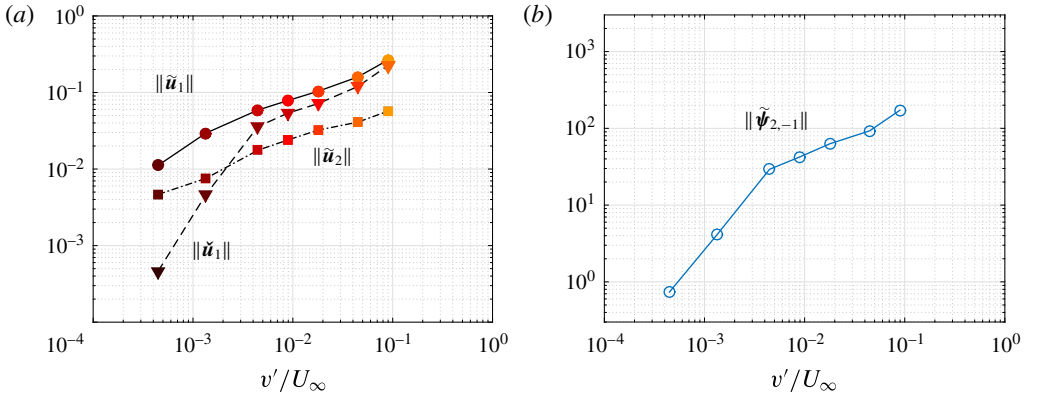

FIGURE 11. (Colour online) (*a*) Norm of the higher harmonic $\widetilde{\boldsymbol{u}}_2$ at $2\omega_1$ (LES), of the response $\widetilde{\boldsymbol{u}}_1$ to the external forcing $\widetilde{\boldsymbol{f}}_1$ at ω_1 (LES), and of the response $\check{\boldsymbol{u}}_1$ to the first Reynolds stress divergence forcing term $\widetilde{\boldsymbol{\psi}}_{2,-1}$ at ω_1 (LNSE). (*b*) Norm of $\widetilde{\boldsymbol{\psi}}_{2,-1}$.

$\widetilde{\boldsymbol{\psi}}_{j,1-j}$ is small, or (ii) if the response to these forcing terms is small. Regarding condition (i), it would be natural to quantify rigorously what 'small $\widetilde{\boldsymbol{\psi}}_{j,1-j}$' means by comparing these forcing terms to the external forcing $\widetilde{\boldsymbol{f}}_1$; however, this is not possible in the present configuration since the $\widetilde{\boldsymbol{\psi}}_{j,1-j}$ are defined in the volume while $\widetilde{\boldsymbol{f}}_1$ is applied at a boundary. Nonetheless, we report for the sake of completeness the norm of $\widetilde{\boldsymbol{\psi}}_{2,-1}$, the first (and likely dominant) Reynolds stress divergence term, in figure 11(*b*). Regarding condition (ii), which may be verified irrespective of condition (i), comparing the response to each forcing term is straightforward; the question is therefore whether the response to the (possibly non-small) Reynolds stress forcing is small compared to the response $\widetilde{\boldsymbol{u}}_1$ to the external forcing:

$$\text{Is } \|\boldsymbol{R}(\omega_1)\widetilde{\boldsymbol{\psi}}_{j,1-j}\| \ll \|\boldsymbol{R}(\omega_1)\widetilde{\boldsymbol{f}}_1\| \,? \tag{4.1}$$

Here we have introduced the resolvent operator $\boldsymbol{R}(\omega) = (\mathrm{i}\omega + \boldsymbol{L}(\overline{\boldsymbol{U}}))^{-1}$. Figure 11(*a*) reports the norm of $\check{\boldsymbol{u}}_1 = \boldsymbol{R}(\omega_1)\widetilde{\boldsymbol{\psi}}_{2,-1}$. At the two lowest forcing amplitudes, $\check{\boldsymbol{u}}_1$ is indeed much smaller than $\widetilde{\boldsymbol{u}}_1$ (in excess of 20 and 5 times, respectively). At larger amplitudes, however, both responses are of the same order of magnitude. At first glance, this seems at odds with the fact that $\widetilde{\boldsymbol{u}}_1$ alone is sufficient to predict the overall coherent fluctuations at ω_1. Interestingly, a closer look reveals that $\check{\boldsymbol{u}}_1$ and $\widetilde{\boldsymbol{u}}_1$ have different phases and therefore cannot interact constructively, meaning that the norm of the response is essentially unaffected by $\check{\boldsymbol{u}}_1$.

4.2. *Optimal response: harnessing the potential for amplification*

Further insight is gained by quantifying how efficiently the two forcing terms (external forcing, and forcing from the interaction of higher harmonics) are amplified. A direct comparison of the gains $\|\widetilde{\boldsymbol{u}}_1\|/\|\widetilde{\boldsymbol{f}}_1\|$ and $\|\check{\boldsymbol{u}}_1\|/\|\widetilde{\boldsymbol{\psi}}_{2,-1}\|$ gives little information, because the forcing terms are defined on a boundary and in the domain, respectively. However, it is possible to assess whether each forcing efficiently exploits the potential for amplification available in the flow. In this context, it is natural to introduce the

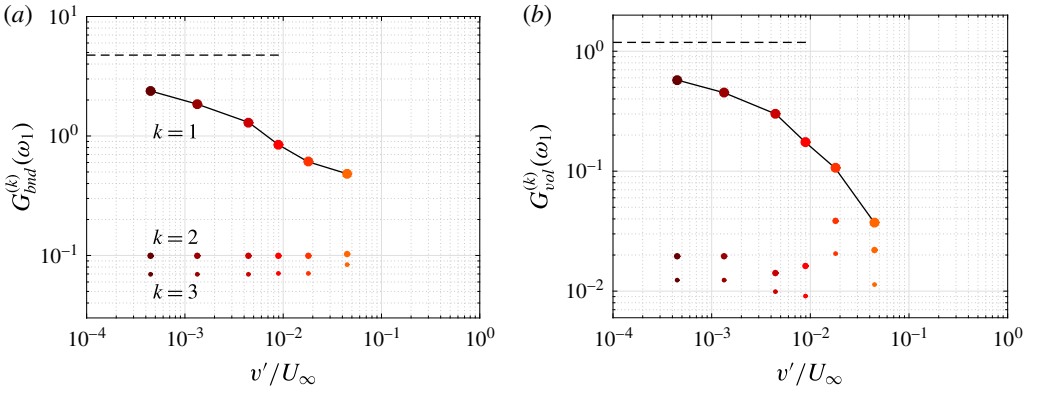

FIGURE 12. (Colour online) First three optimal gains at ω_1, for (*a*) boundary forcing at the cavity end Γ_f, or (*b*) volume forcing in the domain I.

concept of optimal gain, which corresponds to the largest possible linear amplification in the flow at a given frequency: instead of solving

$$(\mathrm{i}\omega + \boldsymbol{L}(\overline{\boldsymbol{U}}))\boldsymbol{u} = \boldsymbol{f} \tag{4.2}$$

to compute the linear response $\boldsymbol{u}$ to a given harmonic forcing $\boldsymbol{f}$ (defined either on a boundary or in the domain), the idea is to identify the optimal forcing $\boldsymbol{f}^{(opt)}$ which maximises the gain

$$G^{(opt)}(\omega) = \max_{\boldsymbol{f}} \frac{\|\boldsymbol{u}\|}{\|\boldsymbol{f}\|} = \frac{\|\boldsymbol{u}^{(opt)}\|}{\|\boldsymbol{f}^{(opt)}\|}. \tag{4.3}$$

With the Euclidean L^2 norm, the optimal gain is the spectral norm of the resolvent operator $\boldsymbol{R}$, which is obtained by performing a singular value decomposition of $\boldsymbol{R}$, or, equivalently, by solving the eigenvalue problem $\boldsymbol{R}^\dagger\boldsymbol{R}\boldsymbol{f} = G^2\boldsymbol{f}$ (where $\boldsymbol{R}^\dagger$ is the adjoint resolvent operator). If needed, the calculation actually yields more, namely an orthogonal set of optimal forcings $\boldsymbol{f}^{(k)}$ and the corresponding set of optimal responses $\boldsymbol{u}^{(k)}$ associated with optimal gains $G^{(k)}$ sorted in decreasing order:

$$G^{(opt)} = G^{(1)} \geqslant G^{(2)} \geqslant G^{(3)} \quad \cdots . \tag{4.4}$$

Examples of resolvent analyses around turbulent mean flows include Farrell & Ioannou (1993), Garnaud *et al.* (2013), McKeon, Sharma & Jacobi (2013) and Beneddine *et al.* (2016).

Figure 12 shows the first three optimal gains for harmonic forcing applied at ω_1 at the cavity end or in the domain. At small forcing amplitudes, the first optimal gain is more than one order of magnitude larger than the following optimal gains, which has been observed in other flows (Dergham, Sipp & Robinet 2013; Boujo & Gallaire 2015; Beneddine *et al.* 2016). At larger amplitudes, this clear separation persists for boundary forcing, while for volume forcing the first optimal forcing becomes increasingly less amplified and is eventually comparable to the following optimal forcings.

In both cases, the first optimal gain decreases with forcing amplitude, indicating that the dominant amplification mechanism weakens as the mean flow is modified. This is confirmed by the optimal volume forcing and optimal response shown in figure 13:

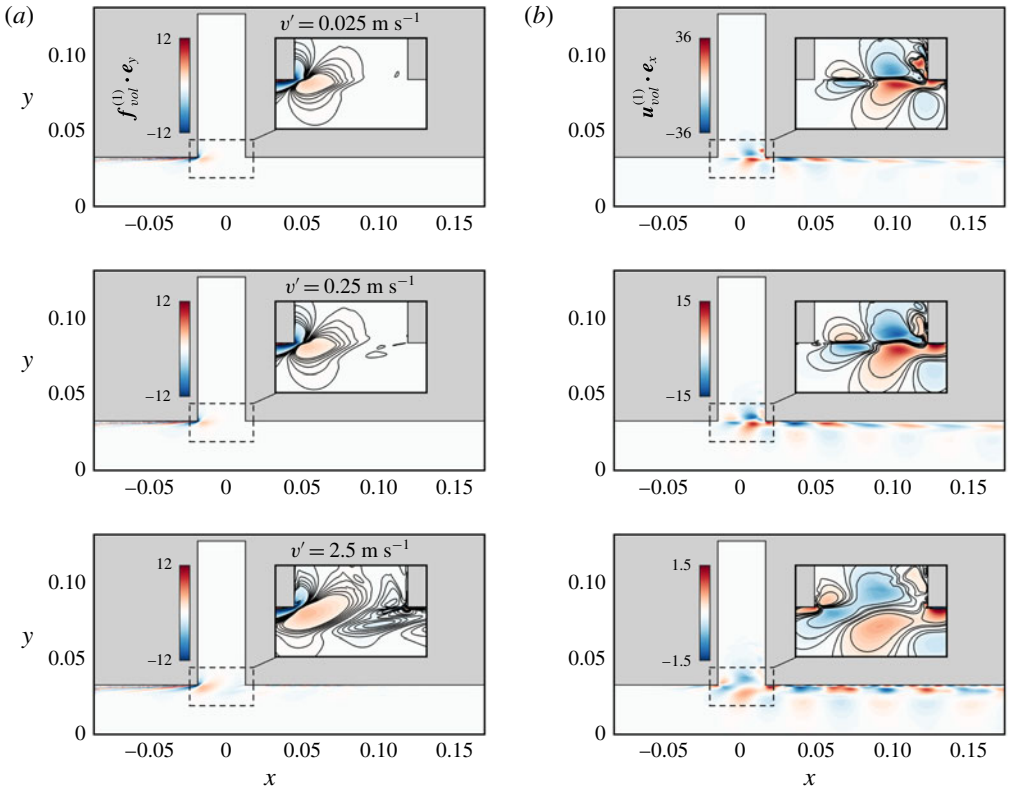

FIGURE 13. (Colour online) (*a*) Optimal volume forcing $\boldsymbol{f}^{(1)}_{vol}$ at ω_1 (unit norm; vertical component). (*b*) Corresponding optimal response $\boldsymbol{u}^{(1)}_{vol}$ (norm $G^{(1)}_{vol}$; streamwise component). Mean flow at forcing amplitudes $v' = 0.025$, 0.25 and 2.5 m s^{-1}.

they clearly identify the mixing layer as the main amplification region, and shear as the main amplification mechanism.

The first three optimal boundary forcings at the cavity end Γ_f are shown in figure 14 for $v' = 0.075$ m s^{-1} (they are essentially independent of v'). They exhibit an increasing number of spatial oscillations over the cavity width. Interestingly, the first optimal is uniform, meaning that the external forcing $\widetilde{\boldsymbol{f}}_1$ considered in this study is actually optimal. The response to the optimal boundary forcing has therefore the same structure as the response to $\widetilde{\boldsymbol{f}}_1$ shown in figure 6. One can observe that the optimal volume response and optimal boundary response have very similar structures at lower and intermediate forcing amplitudes, i.e. when the first optimal gain is much larger than the following optimal gains.

One might wonder whether the volume forcing term from the Reynolds stress divergence $\widetilde{\boldsymbol{\psi}}_{2,-1}$ is close to the optimal volume forcing. For a quantitative answer, let us decompose any forcing $\boldsymbol{f}$ (at a boundary or in the domain) using the optimal forcings ($\boldsymbol{f}^{(k)}_{bnd}$ or $\boldsymbol{f}^{(k)}_{vol}$):

$$\boldsymbol{f} = \sum_{k \geqslant 1} \alpha^{(k)} \boldsymbol{f}^{(k)}. \tag{4.5}$$

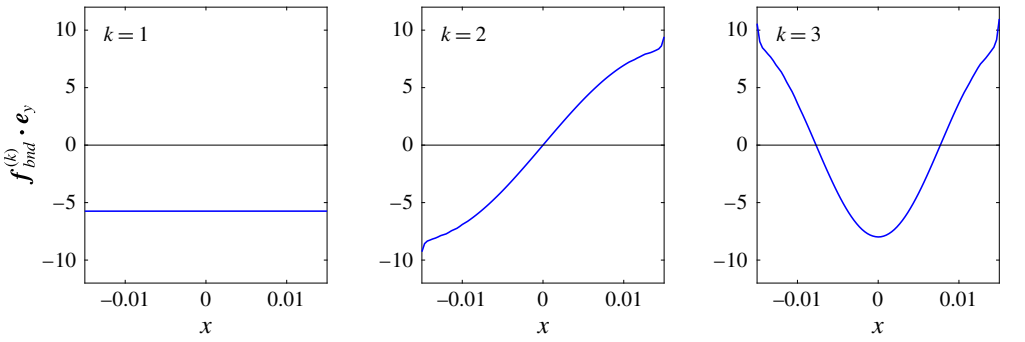

FIGURE 14. (Colour online) First three optimal boundary forcings at the cavity end Γ_f at ω_1 (real part of vertical component of unit-norm $f^{(k)}_{bnd}$). Mean flow forced at amplitude $v'=0.075$ m s^{-1}.

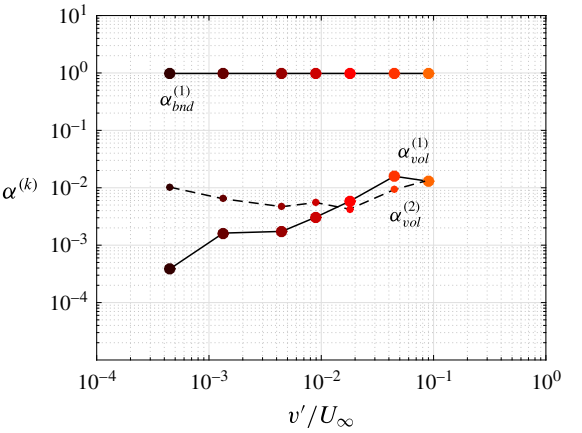

FIGURE 15. (Colour online) Projection coefficients $\alpha^{(k)}$ on the kth optimal volume forcing $f^{(k)}$ at ω_1. Coefficients α_{bnd} and α_{vol} correspond, respectively, to the external forcing $\widetilde{f}_1$ applied at the cavity end, and to the volume Reynolds stress forcing $\widetilde{\psi}_{2,-1}$ resulting from higher-harmonic interactions.

Since the optimal forcings are orthogonal, the coefficients $\alpha^{(k)}_{bnd}$ and $\alpha^{(k)}_{vol}$ are easily expressed in terms of a projection of the considered forcing onto the optimal forcings:

$$\alpha^{(k)}=\frac{(f\,|\,f^{(k)})}{\|f^{(k)}\|^2}. \tag{4.6}$$

With this notation, the projection coefficients for the forcing $\widetilde{f}_1$ at the cavity end are therefore $\alpha^{(1)}_{bnd}=1$, and $\alpha^{(k)}_{bnd}=0$ for $k\geqslant 1$. By contrast, the projection coefficients $\alpha^{(1)}_{vol}$ and $\alpha^{(2)}_{vol}$ for the forcing arising from higher-harmonic interactions are of the order of 10^{-3}–10^{-2} (figure 15), meaning that $\widetilde{\psi}_{2,-1}$ projects very poorly on the first two optimal volume forcings. In other words, the external forcing $\widetilde{f}_1$ harnesses all the amplification available from the cavity end, while $\widetilde{\psi}_{2,-1}$ only benefits from 0.1–1 % of the amplification available in the domain.

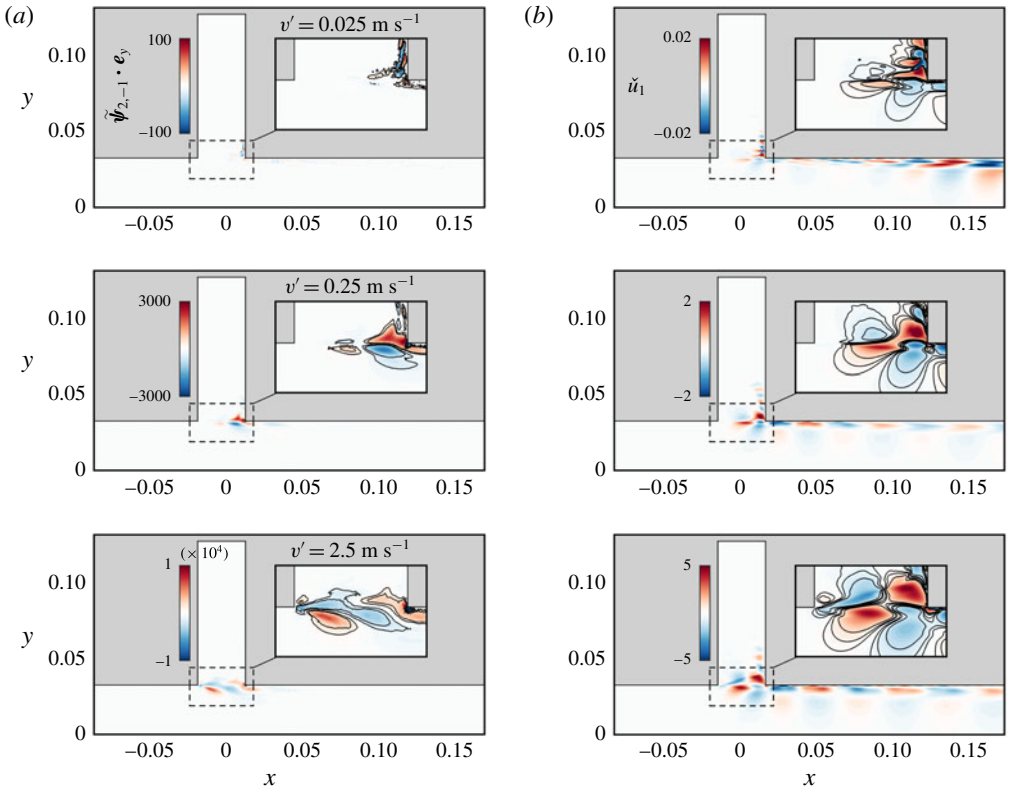

FIGURE 16. (Colour online) (*a*) Reynolds stress divergence $\widetilde{\boldsymbol{\psi}}_{2,-1}$ (vertical component) forcing the flow at ω_1, from LES. (*b*) Linear response $\breve{\boldsymbol{u}}_1$ (streamwise component) to $\widetilde{\boldsymbol{\psi}}_{2,-1}$, from LNSE. External forcing at ω_1, amplitudes $v' = 0.025$, 0.25 and 2.5 m s^{-1}.

One reason for the poor amplification of $\widetilde{\boldsymbol{\psi}}_{2,-1}$ is understood by inspecting its spatial structure in figure 16, and that of $\boldsymbol{f}_{vol}^{(1)}$ in figure 13. At small and intermediate forcing amplitudes, Reynolds stresses are concentrated in the downstream region of the cavity, while the optimal forcing is localised around the upstream corner. At larger forcing amplitudes, the spatial overlap is better but the projection is still small because the structures remain essentially orthogonal: for instance, $\boldsymbol{f}_{vol}^{(1)} \cdot \boldsymbol{e}_y$ is uniform over the whole height of the shear layer, while $\widetilde{\boldsymbol{\psi}}_{2,-1} \cdot \boldsymbol{e}_y$ changes sign above and below.

5. Sensitivity analysis

Using the linear response to harmonic forcing around the mean flow, we have gained understanding about amplification and saturation in the turbulent mixing layer over a deep cavity. It is now natural to investigate flow control in order to reduce or increase the acoustic level. Considering the acoustic forcing $\widetilde{\boldsymbol{f}}_1$ (frequency and spatial shape) as given, one possible strategy is to modify the mean flow $\overline{\boldsymbol{U}}$ (e.g. using wall actuation or a passive control device), which in turn will modify the linear response $\widetilde{\boldsymbol{u}}_1$. How much the gain G is affected by a given flow modification can be found by recomputing the response. However, a systematic study aiming at finding

the most sensitive regions would imply a large computational cost. A more efficient method consists in predicting the effect of any small-amplitude flow modification using adjoint-based sensitivity.

5.1. *Adjoint-based sensitivity: background*

Sensitivity analysis was introduced in the context of hydrodynamic linear stability by Hill (1992), and later used in various parallel (Bottaro, Corbett & Luchini 2003), non-parallel 2D (Giannetti & Luchini 2007; Marquet, Sipp & Jacquin 2008; Meliga, Sipp & Chomaz 2010) and 3D flows (Fani, Camarri & Salvetti 2012) and in thermoacoustic systems (Magri & Juniper 2013) to compute the gradient

$$\nabla_* \lambda = \frac{\mathrm{d}\lambda}{\mathrm{d}*} \tag{5.1}$$

of an eigenvalue $\lambda = \sigma + \mathrm{i}\omega$ with respect to a variety of modifications $(*)$: (i) steady flow modification, (ii) steady volume/boundary control, and (iii) hypothetical localised 'velocity-to-force' feedback ('structural sensitivity') (see Chomaz (2005) for more details about structural sensitivity, and Luchini & Bottaro (2014) for a broad review about adjoint equations). The gradient (5.1) is useful information since it immediately predicts, via a simple scalar product, the first-order variation $\lambda \to \lambda + \delta\lambda$ induced by any small-amplitude modification: for instance, a flow modification $\boldsymbol{U} \to \boldsymbol{U} + \boldsymbol{\delta U}$ induces an eigenvalue variation

$$\delta\lambda = (\nabla_{\boldsymbol{U}} \lambda \mid \boldsymbol{\delta U}) = \left(\frac{\mathrm{d}\lambda}{\mathrm{d}\boldsymbol{U}} \,\middle|\, \boldsymbol{\delta U} \right). \tag{5.2}$$

For linearly stable flows, Brandt *et al.* (2011) extended sensitivity analysis to the linear response to harmonic volume forcing. They found that the sensitivity of the (squared) harmonic gain G^2 with respect to a modification of the flow $\boldsymbol{U}$ (case (i) above) is given by

$$\nabla_{\boldsymbol{U}} G^2_{vol} = 2G^2_{vol}\, \mathrm{Re}\{-\nabla \boldsymbol{u}^{\mathrm{H}} \cdot \boldsymbol{f}_{vol} + \nabla \boldsymbol{f}_{vol} \cdot \boldsymbol{u}^*\}, \tag{5.3}$$

where $\boldsymbol{u}$ is the response to the volume forcing $\boldsymbol{f}_{vol}$, and $(\cdot)^{\mathrm{H}}$ denotes Hermitian transpose (conjugate transpose). Boujo & Gallaire (2015) considered boundary forcing $\boldsymbol{f}_{bnd}$, in which case the sensitivity of the harmonic gain to flow modification is

$$\nabla_{\boldsymbol{U}} G^2_{bnd} = 2\,\mathrm{Re}\{-\nabla \boldsymbol{u}^{\mathrm{H}} \cdot \boldsymbol{u}^\dagger + \nabla \boldsymbol{u}^\dagger \cdot \boldsymbol{u}^*\}, \tag{5.4}$$

where $\boldsymbol{u}$ is the response to the boundary forcing $\boldsymbol{f}_{bnd}$, and the adjoint perturbation $\boldsymbol{u}^\dagger$ is a solution of the adjoint resolvent problem with $\boldsymbol{u}$ as volume forcing (see appendix B for details). From the knowledge of (5.3) or (5.4), one can proceed to compute the sensitivity to control (case (ii) above).

Recently, Qadri & Schmid (2017) proposed an equivalent to structural sensitivity (case (iii) above) for the amplification of harmonic volume forcing. Rearranging their expression, the overall gain variation for a unit feedback localised in $\boldsymbol{x} = \boldsymbol{x}_0$ can be recast as

$$\delta(G^2_{vol}) = -2G^2_{vol}\, \mathrm{Re}\{\boldsymbol{f}_{vol}(\boldsymbol{x}_0) \cdot \boldsymbol{u}(\boldsymbol{x}_0)\}. \tag{5.5}$$

When considering boundary forcing, an additional intermediate step is necessary: in this case, the gain variation for a localised unit feedback is

$$\delta(G^2_{bnd}) = -2\,\mathrm{Re}\{\boldsymbol{u}^\dagger(\boldsymbol{x}_0) \cdot \boldsymbol{u}(\boldsymbol{x}_0)\}, \tag{5.6}$$

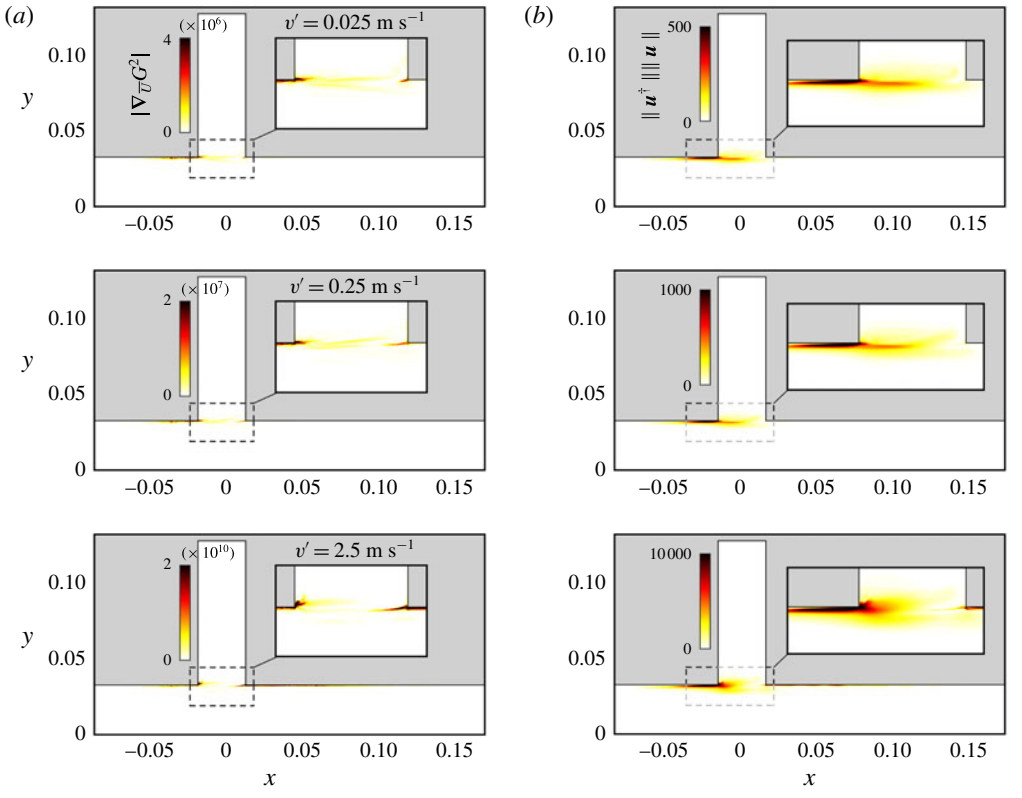

FIGURE 17. (Colour online) Sensitivity of the linear optimal gain $G^2_{opt}(\omega_1)$, for harmonic forcing at the cavity end Γ_f. (*a*) Magnitude of the sensitivity with respect to mean flow modification (5.4). (*b*) Structural sensitivity (5.6), i.e. sensitivity with respect to a localised feedback. Forcing amplitudes $v' = 0.025$, 0.25 and 2.5 m s^{-1}.

where, again, $\boldsymbol{u}^\dagger$ is a solution of the adjoint resolvent problem with $\boldsymbol{u}$ as volume forcing (see details in appendix B). A simple way to analyse the sensitivity of the harmonic gain with respect to localised feedback is to look at the space-dependent product

$$\|\boldsymbol{f}_{vol}(\boldsymbol{x}_0)\| \, \|\boldsymbol{u}(\boldsymbol{x}_0)\| \quad \text{or} \quad \|\boldsymbol{u}^\dagger(\boldsymbol{x}_0)\| \, \|\boldsymbol{u}(\boldsymbol{x}_0)\|, \tag{5.7a,b}$$

which is analogous to the structural sensitivity of an eigenvalue (product of the direct and adjoint modes).

5.2. *Sensitivity of the optimal gain*

In the following we investigate the sensitivity of the optimal harmonic gain for boundary forcing at the cavity end Γ_f, at frequency ω_1. The sensitivity to mean flow modification (5.4) and structural sensitivity (5.6) are shown in figure 17. Both reach their largest magnitude in a localised region near the upstream cavity corner (and, to a lesser extent, in the boundary layer upstream of the cavity as well as in the mixing layer; a second region of large sensitivity appears at the downstream corner as the forcing amplitude v' increases). Therefore, the linear amplification between optimal boundary forcing and optimal response is the most sensitive to modifications near the upstream corner.

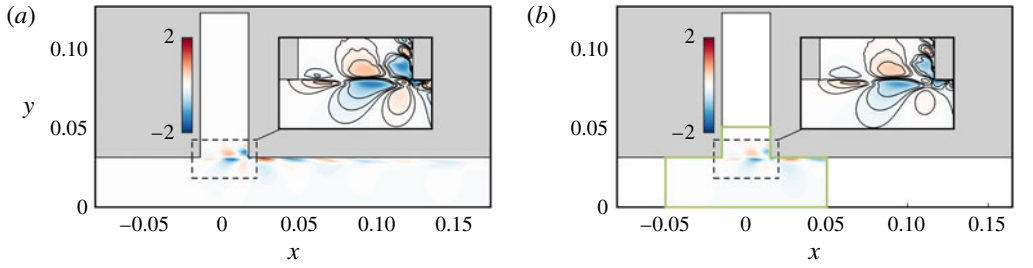

FIGURE 18. (Colour online) Effect of the size of the LNSE domain used to compute the linear response (frequency ω_1, forcing amplitude $v' = 0.075$ m s^{-1}). (*a*) Reference domain I. (*b*) Smaller domain D_3^{xy}.

This is consistent with the fact that most of the amplification is driven by the mean shear: acoustic forcing induces perturbations near the upstream corner, which are then amplified in the mixing layer. Any control aiming at modifying the amplification should therefore target the upstream corner. This also explains why saturation is more marked once fluctuations (Reynolds stresses) have moved upstream, in the region where the mean flow is more sensitive to their effect.

We recall from § 4.2 that (i) the responses to optimal boundary and volume forcing are very similar (in terms of spatial structure), and that (ii) the first optimal gain is almost always much larger than the following optimal gains. These two elements point to a robust amplification mechanism in the mixing layer, fairly insensitive to the exact shape and location of the forcing. In addition, we note that the adjoint perturbation $\boldsymbol{u}^\dagger$ in the sensitivities (5.4) and (5.6) looks similar to the optimal response $\boldsymbol{f}^{(opt)}$, which leads to large sensitivities in exactly the same regions for volume forcing (not shown) and boundary forcing (figure 17).

Finally, we observe that the linear gain does not vary substantially when reducing the size of the computational domain, as long as the boundaries are not too close to the region of large structural sensitivity (see details in appendix C). The spatial structure of the response is unaffected too (figure 18). This is in agreement with Giannetti & Luchini (2007), who found a similar behaviour for the leading eigenvalue and eigenmode of the flow past a circular cylinder at $Re = 50$: they hypothesised that 'the characteristics of the global mode are dictated mainly by the conditions existing in the region where values of [structural sensitivity] substantially different from zero are attained', i.e. where the global mode and associated adjoint mode overlap. We formulate the same hypothesis in the case of harmonic amplification: the value of the linear gain and the spatial structure of the response are dictated mainly by the flow in the region where structural sensitivity is not small, i.e. where the response $\boldsymbol{u}$ and the volume forcing $\boldsymbol{f}$ (or the adjoint perturbation $\boldsymbol{u}^\dagger$ associated with boundary forcing) overlap.

6. Conclusion

We consider the turbulent flow over a deep cavity and compute the linear response to a uniform harmonic forcing applied at the cavity end. This forcing mimics a plane acoustic wave corresponding to the dominant acoustic resonance mode (quarter-wave mode) at frequency ω_1. Calculations are carried out in the framework of the incompressible linearised Navier–Stokes equations (LNSE) with an eddy-viscosity

turbulence model, and using as linearisation point the mean flow obtained from nonlinear large-eddy simulations (LES) with a similar harmonic forcing at several amplitudes spanning more than two orders of magnitude. The influence of higher harmonics on the mean flow is automatically accounted for via LES, while their influence on coherent oscillations at ω_1 is neglected. The aim of the work is to assess the ability of this LNSE-based procedure to yield accurate results in terms of spatial structure and response amplitude, and to capture the saturation mechanism that, ultimately, would set the limit-cycle oscillation amplitude in a self-excited aeroacoustic resonance.

We find that the response amplitude is well predicted, both with a hydrodynamic measure (kinetic energy) and with an acoustic measure (Coriolis force involved in acoustic power generation). Vortical structures in the shear layer are in good agreement too, except at very large forcing amplitudes. The gain (amplification of the forcing) is largest in the unforced case and decreases with forcing amplitude. This is consistent with the following saturation scenario: as the amplitude of oscillations grows, their nonlinear interaction (in the form of Reynolds stresses) modifies the mean flow, and shear-driven amplification in the thickened shear layer is reduced.

We also note with a resolvent analysis that the optimal boundary forcing (i.e. the forcing which undergoes the largest possible amplification) at the cavity end is uniform, i.e. the forcing we prescribe in our study has precisely the optimal shape and benefits from the entire potential for amplification available at the cavity end. By contrast, the nonlinear interaction of the first and second harmonics which forces the flow at ω_1 projects poorly on the optimal volume forcing and does not take advantage efficiently of the potential for amplification available in the domain. This is partly due to a separation of singular values of the resolvent (first and following optimal gains); although this may not hold at other frequencies, it is relevant in the context of aeroacoustic resonances where the acoustic frequency is close to that of a marginally stable hydrodynamic eigenmode.

Finally, sensitivity analysis identifies the upstream boundary layer and upstream cavity corner as regions where both localised feedback and mean flow modification have the largest effect on harmonic amplification, information that can contribute to a systematic and computationally inexpensive control design.

We observe that there is a good agreement between LES and LNSE harmonic gains, even though the higher harmonics neglected in the LNSE are not small. This seems to suggest that the mean flow contains all important nonlinearities. The influence of nonlinearities contained in the turbulence model is not negligible, but somewhat limited at the frequency of interest. That higher harmonics can be neglected is by no means general and requires either (i) that their nonlinear interactions (coherent Reynolds stresses) are small, or (ii) that the harmonic response of the mean flow to these Reynolds stresses is substantially smaller than the response to the external forcing. It can be expected that condition (i) will not be verified in general in several flows, especially at large forcing amplitudes. Condition (ii) is more likely to be verified when the external forcing is efficiently amplified, and/or when coherent Reynolds stresses are poorly amplified. Considering their projection on the optimal forcing is a convenient way to assess this last property, provided there is a clear separation of optimal gains. In flows where this separation is not observed, one should not expect *a priori* a linearised harmonic response calculation to predict correctly the amplitude and structure of coherent fluctuations.

A future goal is to extend the method to the prediction of limit-cycle amplitudes in self-excited aeroacoustic resonances. This should be accomplished in a stand-alone

	M_1	M_2	**M_3**	M_4
N_{SL}	315	420	**525**	630
N_v	60 743	103 045	**166 464**	230 240
N_e	120 214	204 388	**330 794**	457 921

TABLE 1. Meshes used for the convergence study: number of vertices across the shear layer, total number of vertices and total number of triangular elements. M_3 in bold is the mesh used throughout the paper.

fashion, i.e. without relying on expensive nonlinear simulations such as LES to compute the mean flow *a priori*. Extending semi-linear self-consistent models (Mantič-Lugo *et al.* 2014; Mantič-Lugo & Gallaire 2016) to turbulent flows would, if technically possible, constitute a promising method.

Acknowledgements

E.B. and N.N. acknowledge support by Repower and the ETH Zürich Foundation. We also thank the anonymous reviewers for helpful comments and suggestions.

Appendix A. Convergence study on mesh size

The influence of the mesh size on the LNSE results is analysed with a convergence study involving four meshes, M_1–M_4. All meshes share the same structure: coarser at the inlet and outlet, and gradually finer towards the shear layer. Mesh M_1 contains $N_{SL} = 315$ vertices across the shear layer $\{-W/2 \leqslant x \leqslant W/2,\ y = D/2\}$, resulting in approximately $N_e = 120\,000$ triangular elements in the whole domain I. Meshes M_2 to M_4 are obtained by applying to M_1 a uniform refinement of factor 1.33, 1.67 and 2, resulting in approximately $N_e = 204\,000$, $331\,000$ and $458\,000$ elements, respectively (table 1).

Convergence is reported in figure 19 for two selected quantities: harmonic gain G_{bnd} for boundary forcing $\widetilde{\boldsymbol{f}}_1$ on Γ_f, and first optimal gain $G^{(1)}_{vol}$ for volume forcing in I (both at frequency ω_1, around the LES mean flow at $v' = 0.075$ m s^{-1}). While G_{bnd} is already well converged on the relatively coarser mesh M_1 (0.3 % variation between M_1 and M_4), $G^{(1)}_{vol}$ requires the finer mesh M_3 for a satisfactory convergence (0.9 % variation between M_3 and M_4). As mentioned in § 3.2, mesh M_3 is therefore used throughout the paper.

Appendix B. Sensitivity of harmonic gain

Recall the LNSE (3.14) and the definition of the resolvent operator:

$$(\mathrm{i}\omega + \boldsymbol{L})\boldsymbol{u} = \boldsymbol{f} \quad \Longleftrightarrow \quad \boldsymbol{u} = (\mathrm{i}\omega + \boldsymbol{L})^{-1}\boldsymbol{f} = \boldsymbol{R}(\omega)\boldsymbol{f}. \tag{B 1}$$

For the sake of simplicity and generality, we drop tildes $\widetilde{\cdot}$ and omit the dependence on the mean flow $\overline{\boldsymbol{U}}$. We distinguish two cases: harmonic forcing $\boldsymbol{f}_{vol}$ applied in the volume,

$$(\mathrm{i}\omega + \boldsymbol{L})\boldsymbol{u}_{vol} = \boldsymbol{f}_{vol} \quad \text{in } I, \quad \boldsymbol{u}_{vol} = \boldsymbol{0} \quad \text{on } \Gamma_f, \tag{B 2}$$

and harmonic forcing $\boldsymbol{f}_{bnd}$ applied at a boundary,

$$(\mathrm{i}\omega + \boldsymbol{L})\boldsymbol{u}_{bnd} = \boldsymbol{0} \quad \text{in } I, \quad \boldsymbol{u}_{bnd} = \boldsymbol{f}_{bnd} \quad \text{on } \Gamma_f. \tag{B 3}$$

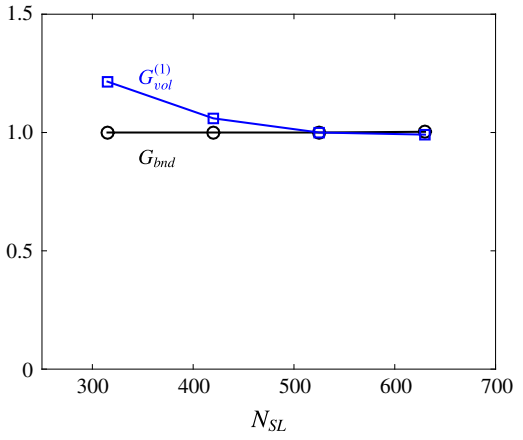

FIGURE 19. (Colour online) Influence of mesh size: convergence with N_{SL}, the number of vertices across the shear layer (i.e. along the line $\{-W/2 \leqslant x \leqslant W/2, y = D/2\}$). Circles, harmonic gain for boundary forcing on Γ_f; squares, first optimal gain for volume forcing in I. Gains are normalised by their values obtained on the reference mesh M_3 ($N_{SL} = 525$, see table 1). Forcing frequency ω_1, amplitude $v' = 0.075$ m s^{-1}.

We write those two problems in short as

$$\boldsymbol{u}_{vol} = \boldsymbol{R}_{vol}\boldsymbol{f}_{vol} \quad \text{and} \quad \boldsymbol{u}_{bnd} = \boldsymbol{R}_{bnd}\boldsymbol{f}_{bnd}. \tag{B 4a,b}$$

For a given forcing $\boldsymbol{f}$, a variation of the NS operator $\boldsymbol{L} \to \boldsymbol{L} + \boldsymbol{\delta L}$ induces a variation of the response $\boldsymbol{u} \to \boldsymbol{u} + \boldsymbol{\delta u}$. Substituting into (B 2) and (B 3), expanding and keeping only zeroth- and first-order terms yields for volume forcing

$$(\mathrm{i}\omega + \boldsymbol{L})\boldsymbol{u}_{vol} + (\mathrm{i}\omega + \boldsymbol{L})\boldsymbol{\delta u}_{vol} + \boldsymbol{\delta L}\,\boldsymbol{u}_{vol} = \boldsymbol{f}_{vol} \quad \text{in } I, \quad \boldsymbol{u}_{vol} + \boldsymbol{\delta u}_{vol} = \boldsymbol{0} \quad \text{on } \Gamma_f, \tag{B 5}$$

and for boundary forcing

$$(\mathrm{i}\omega + \boldsymbol{L})\boldsymbol{u}_{bnd} + (\mathrm{i}\omega + \boldsymbol{L})\boldsymbol{\delta u}_{bnd} + \boldsymbol{\delta L}\,\boldsymbol{u}_{bnd} = \boldsymbol{0} \quad \text{in } I, \quad \boldsymbol{u}_{bnd} + \boldsymbol{\delta u}_{bnd} = \boldsymbol{f}_{bnd} \quad \text{on } \Gamma_f. \tag{B 6}$$

Upon subtracting (B 2) and (B 3), respectively, both problems reduce to:

$$(\mathrm{i}\omega + \boldsymbol{L})\boldsymbol{\delta u} = -\boldsymbol{\delta L}\,\boldsymbol{u} \quad \text{in } I, \quad \boldsymbol{\delta u} = \boldsymbol{0} \quad \text{on } \Gamma_f. \tag{B 7}$$

That is, in both cases (volume forcing and boundary forcing), the response variation $\boldsymbol{\delta u}$ is solution of a volume resolvent problem (volume forcing $-\boldsymbol{\delta L}\,\boldsymbol{u}$ and homogeneous boundary conditions):

$$\boldsymbol{\delta u}_{vol} = -\boldsymbol{R}_{vol}\boldsymbol{\delta L}_{vol}\boldsymbol{u}_{vol} \quad \text{and} \quad \boldsymbol{\delta u}_{bnd} = -\boldsymbol{R}_{vol}\boldsymbol{\delta L}_{bnd}\boldsymbol{u}_{bnd}. \tag{B 8a,b}$$

We now proceed to find the gain variation induced by the variation of the NS operator. The variation of the gain

$$G^2 = \frac{\|\boldsymbol{u}\|^2}{\|\boldsymbol{f}\|^2} = \frac{(\boldsymbol{u} \mid \boldsymbol{u})}{(\boldsymbol{f} \mid \boldsymbol{f})}, \tag{B 9}$$

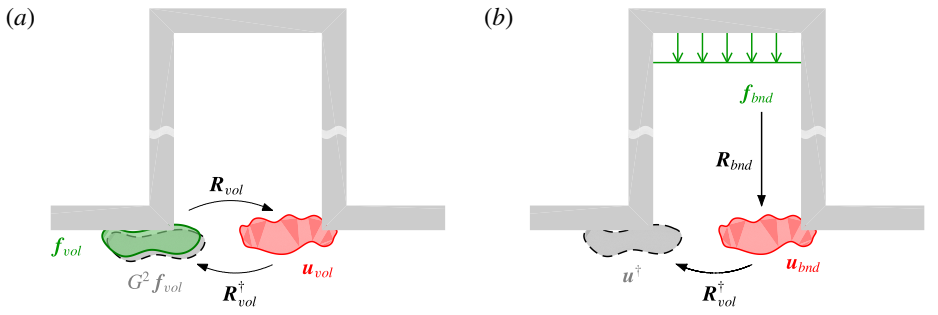

FIGURE 20. (Colour online) (*a*) Harmonic volume forcing $\boldsymbol{f}_{vol}$ and associated response $\boldsymbol{u}_{vol}$, from which one can compute the gain sensitivities (5.3) and (5.5). (*b*) Harmonic boundary forcing $\boldsymbol{f}_{bnd}$ and associated response $\boldsymbol{u}_{bnd}$. The adjoint $\boldsymbol{u}^{\dagger}$ is needed to compute the gain sensitivities (5.4) and (5.6).

reads at zeroth and first orders:

$$G^2 + \delta(G^2) = \frac{(\boldsymbol{u}+\boldsymbol{\delta u} \mid \boldsymbol{u}+\boldsymbol{\delta u})}{(\boldsymbol{f} \mid \boldsymbol{f})} = \frac{(\boldsymbol{u} \mid \boldsymbol{u})}{(\boldsymbol{f} \mid \boldsymbol{f})} + 2\,\mathrm{Re}\left\{\frac{(\boldsymbol{u} \mid \boldsymbol{\delta u})}{(\boldsymbol{f} \mid \boldsymbol{f})}\right\}, \tag{B 10}$$

i.e. after subtracting (B 9) and multiplying by $\|\boldsymbol{f}\|^2$:

$$\delta(G^2)\|\boldsymbol{f}\|^2 = 2\,\mathrm{Re}\{(\boldsymbol{u} \mid \boldsymbol{\delta u})\}. \tag{B 11}$$

Substituting the response variation $\boldsymbol{\delta u}$ (B 8), and using the definition of an adjoint operator, one obtains for volume forcing

$$\begin{aligned}\delta(G_{vol}^2)\|\boldsymbol{f}_{vol}\|^2 &= 2\,\mathrm{Re}\{(\boldsymbol{u}_{vol} \mid -\boldsymbol{R}_{vol}\boldsymbol{\delta L}_{vol}\boldsymbol{u}_{vol})\}\\ &= -2\,\mathrm{Re}\{(\boldsymbol{R}_{vol}^{\dagger}\boldsymbol{u}_{vol} \mid \boldsymbol{\delta L}_{vol}\boldsymbol{u}_{vol})\}\\ &= -2\,\mathrm{Re}\{(G_{vol}^2\boldsymbol{f}_{vol} \mid \boldsymbol{\delta L}_{vol}\boldsymbol{u}_{vol})\},\end{aligned} \tag{B 12}$$

and for inlet forcing

$$\begin{aligned}\delta(G_{bnd}^2)\|\boldsymbol{f}_{bnd}\|^2 &= 2\,\mathrm{Re}\{(\boldsymbol{u}_{bnd} \mid -\boldsymbol{R}_{vol}\boldsymbol{\delta L}_{bnd}\boldsymbol{u}_{bnd})\}\\ &= -2\,\mathrm{Re}\{(\boldsymbol{R}_{vol}^{\dagger}\boldsymbol{u}_{bnd} \mid \boldsymbol{\delta L}_{bnd}\boldsymbol{u}_{bnd})\}\\ &= -2\,\mathrm{Re}\{(\boldsymbol{u}^{\dagger} \mid \boldsymbol{\delta L}_{bnd}\boldsymbol{u}_{bnd})\}.\end{aligned} \tag{B 13}$$

In (B 12) we have used the relation $\boldsymbol{R}_{vol}^{\dagger}\boldsymbol{u}_{vol} = G_{vol}^2\boldsymbol{f}_{vol}$ (Brandt *et al.* 2011; Boujo & Gallaire 2015). In (B 13), however, we have introduced $\boldsymbol{u}^{\dagger} = \boldsymbol{R}_{vol}^{\dagger}\boldsymbol{u}_{bnd}$ (defined in the domain), which is not equal to $G_{bnd}^2\boldsymbol{f}_{bnd}$ (defined on the boundary). Note that one can choose a unit forcing, $\|\boldsymbol{f}\| = 1$, since the gain is linear.

As illustrated in figure 20, knowing $\boldsymbol{f}_{vol}$ and $\boldsymbol{u}_{vol}$ is sufficient to compute the gain sensitivity in the case of volume forcing; the adjoint $\boldsymbol{u}^{\dagger}$ is necessary, however, to compute the gain sensitivity in the case of boundary forcing.

Expressions (B 12) and (B 13) allow one to easily compute gain variations $\delta(G^2)$ for any small-amplitude modification $\boldsymbol{\delta L}$ of the NS operator, without solving explicitly for the modified response $\boldsymbol{u}+\boldsymbol{\delta u}$. These expressions are general, but we can now make them more specific for two particular modifications $\boldsymbol{\delta L}$ of interest.

	REF (I)	D_1^x	D_2^x	D_3^x	D_1^y	D_2^y	D_3^y	D_4^y	D_1^{xy}	D_2^{xy}	D_3^{xy}
x_1	**−80**	−40	−30	−20	—	—	—	—	−50	−50	−50
x_2	**165**	40	30	20	—	—	—	—	50	50	50
y_2	**121**	—	—	—	80	50	40	40	80	50	50
y_1	**−31**	—	—	—	—	0	10	20	—	—	0

TABLE 2. Domains used for convergence study, with various locations of the inlet (x_1), outlet (x_2), cavity end (y_2) and lower channel wall (y_1). Dimensions in mm. Only values different from the reference domain I are indicated. See also figure 21.

First, when the mean flow is modified, $\overline{U} \to \overline{U} + \delta\overline{U}$, the NS operator variation reads

$$\delta \boldsymbol{L}\, \boldsymbol{u} = (\boldsymbol{u} \cdot \nabla)\delta\overline{\boldsymbol{U}} + (\delta\overline{\boldsymbol{U}} \cdot \nabla)\boldsymbol{u}, \tag{B 14}$$

and one obtains, after a few manipulations,

$$\begin{aligned} \delta(G^2_{vol}) &= -2G^2_{vol}\,\mathrm{Re}\{(\boldsymbol{f}_{vol} \mid (\boldsymbol{u}_{vol} \cdot \nabla)\delta\overline{\boldsymbol{U}} + (\delta\overline{\boldsymbol{U}} \cdot \nabla)\boldsymbol{u}_{vol})\} \\ &= -2G^2_{vol}\,\mathrm{Re}\{(\nabla \boldsymbol{u}^{\mathrm{H}}_{vol} \cdot \boldsymbol{f}_{vol} - \nabla \boldsymbol{f}_{vol} \cdot \boldsymbol{u}^*_{vol} \mid \delta\overline{\boldsymbol{U}})\}, \qquad \text{(B 15}a\text{)} \\ \delta(G^2_{bnd}) &= -2\,\mathrm{Re}\{(\boldsymbol{u}^\dagger \mid (\boldsymbol{u}_{bnd} \cdot \nabla)\delta\overline{\boldsymbol{U}} + (\delta\overline{\boldsymbol{U}} \cdot \nabla)\boldsymbol{u}_{bnd})\} \\ &= -2\,\mathrm{Re}\{(\nabla \boldsymbol{u}^{\mathrm{H}}_{bnd} \cdot \boldsymbol{u}^\dagger - \nabla \boldsymbol{u}^\dagger \cdot \boldsymbol{u}^*_{bnd} \mid \delta\overline{\boldsymbol{U}})\}, \qquad \text{(B 15}b\text{)} \end{aligned}$$

hence the expressions (5.3) and (5.4) of the gain sensitivity $\nabla_{\overline{U}} G^2$.

Second, for a feedback localised in $\boldsymbol{x} = \boldsymbol{x}_0$ in the form of a 'velocity-to-force' coupling, the NS operator variation reads

$$\delta \boldsymbol{L}\, \boldsymbol{u} = \boldsymbol{C}(\boldsymbol{x})\boldsymbol{u} = \delta(\boldsymbol{x} - \boldsymbol{x}_0)\boldsymbol{C}_0\boldsymbol{u}, \tag{B 16}$$

where $\delta(\boldsymbol{x})$ is the 2D delta Dirac function. Expressions (B 12) and (B 13) therefore become

$$\begin{aligned} \delta(G^2_{vol}) &= -2G^2_{vol}\,\mathrm{Re}\{(\boldsymbol{f}_{vol} \mid \delta(\boldsymbol{x} - \boldsymbol{x}_0)\boldsymbol{C}_0\boldsymbol{u}_{vol})\} \\ &= -2G^2_{vol}\,\mathrm{Re}\{\boldsymbol{f}_{vol}(\boldsymbol{x}_0) \cdot \boldsymbol{C}_0\boldsymbol{u}_{vol}(\boldsymbol{x}_0)\}, \qquad \text{(B 17}a\text{)} \\ \delta(G^2_{bnd}) &= -2\,\mathrm{Re}\{(\boldsymbol{u}^\dagger \mid \delta(\boldsymbol{x} - \boldsymbol{x}_0)\boldsymbol{C}_0\boldsymbol{u}_{bnd})\} \\ &= -2\,\mathrm{Re}\{\boldsymbol{u}^\dagger(\boldsymbol{x}_0) \cdot \boldsymbol{C}_0\boldsymbol{u}_{bnd}(\boldsymbol{x}_0)\}. \qquad \text{(B 17}b\text{)} \end{aligned}$$

Choosing the identity matrix for $\boldsymbol{C}_0$ (i.e. a velocity sensed in the x (respectively y) direction results in a force in the x (respectively y) direction only), one recovers the expressions (5.5) and (5.6) of the gain sensitivity $\nabla_{\boldsymbol{fb}} G^2$.

Appendix C. Influence of domain size

A series of smaller LNSE domains are used to investigate which flow regions are important to capture the linear response to harmonic forcing. Only the LNSE domain is modified: all linear response calculations are performed with the same LES mean flow. The positions of the boundaries are varied as follows (see table 2): inlet (x_1) and outlet (x_2) in domains D^x, cavity end (y_2) and lower channel wall (y_1) in domains D^y, and all four boundaries in domains D^{xy}. Note that the uniform harmonic forcing $\boldsymbol{f}$ is applied on Γ_f, whose position y_2 varies in domains D^y and D^{xy}.

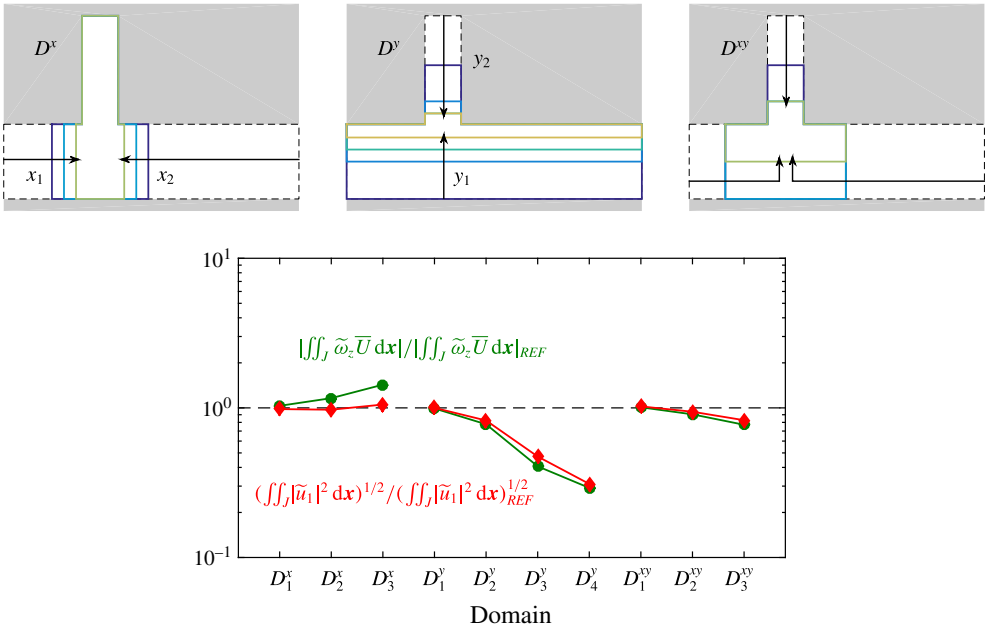

FIGURE 21. (Colour online) Influence of domain size. Linear harmonic response to boundary forcing on Γ_f. Circles, kinetic energy (3.17); diamonds, vertical component of the Coriolis force (3.18). Linear response values are normalised by the values obtained on the largest reference domain I (see table 2). Forcing frequency ω_1, amplitude $v' = 0.075$ m s^{-1}.

The response measured in terms of kinetic energy (3.17) and vertical component of the Coriolis force (3.18) is shown in figure 21 (normalised by values obtained on the largest reference domain I). Note that domains D^y and D^{xy} have a smaller vertical extension than region J, where the response is normally computed.

REFERENCES

ÅKERVIK, E., HŒPFFNER, J., EHRENSTEIN, U. & HENNINGSON, D. 2007 Optimal growth, model reduction and control in a separated boundary-layer flow using global eigenmodes. *J. Fluid Mech.* **579**, 305–314.

DEL ÁLAMO, J. C. & JIMÉNEZ, J. 2006 Linear energy amplification in turbulent channels. *J. Fluid Mech.* **559**, 205–213.

ALVAREZ, J. O., KERSCHEN, E. J. & TUMIN, A. 2004 A theoretical model for cavity acoustic resonances in subsonic flow. In *10th AIAA/CEAS Aeroacoustics Conference*. American Institute of Aeronautics and Astronautics.

BARBAGALLO, A., SIPP, D. & SCHMID, P. J. 2009 Closed-loop control of an open cavity flow using reduced-order models. *J. Fluid Mech.* **641**, 1–50.

BARKLEY, D. 2006 Linear analysis of the cylinder wake mean flow. *Europhys. Lett.* **75** (5), 750–756.

BENEDDINE, S., SIPP, D., ARNAULT, A., DANDOIS, J. & LESSHAFFT, L. 2016 Conditions for validity of mean flow stability analysis. *J. Fluid Mech.* **798**, 485–504.

BOTTARO, A., CORBETT, P. & LUCHINI, P. 2003 The effect of base flow variation on flow stability. *J. Fluid Mech.* **476**, 293–302.

BOUJO, E., EHRENSTEIN, U. & GALLAIRE, F. 2013 Open-loop control of noise amplification in a separated boundary layer flow. *Phys. Fluids* **25** (12), 124106.

BOUJO, E. & GALLAIRE, F. 2015 Sensitivity and open-loop control of stochastic response in a noise amplifier flow: the backward-facing step. *J. Fluid Mech.* **762**, 361–392.

BRANDT, L., SIPP, D., PRALITS, J. O. & MARQUET, O. 2011 Effect of base-flow variation in noise amplifiers: the flat-plate boundary layer. *J. Fluid Mech.* **687**, 503–528.

CAIN, A. B., BOWER, W. W., MCCOTTER, F. & ROMER, W. W. 1996 Modeling and prediction of weapons bay acoustic amplitude and frequency. *Tech. Rep.* VEDA Inc.

CHOMAZ, J. M. 2005 Global instabilities in spatially developing flows: non-normality and nonlinearity. *Annu. Rev. Fluid Mech.* **37**, 357–392.

DERGHAM, G., SIPP, D. & ROBINET, J.-CH. 2013 Stochastic dynamics and model reduction of amplifier flows: the backward facing step flow. *J. Fluid Mech.* **719**, 406–430.

EDSTRAND, A. M., DAVIS, T. B., SCHMID, P. J., TAIRA, K. & CATTAFESTA, L. N. 2016 On the mechanism of trailing vortex wandering. *J. Fluid Mech.* **801**, R1.

FANI, A., CAMARRI, S. & SALVETTI, M. V. 2012 Stability analysis and control of the flow in a symmetric channel with a sudden expansion. *Phys. Fluids* **24** (8), 084102.

FARRELL, B. F. & IOANNOU, P. J. 1993 Stochastic forcing of the linearized Navier–Stokes equations. *Phys. Fluids* A **5** (11), 2600–2609.

GARNAUD, X., LESSHAFFT, L., SCHMID, P. J. & HUERRE, P. 2013 The preferred mode of incompressible jets: linear frequency response analysis. *J. Fluid Mech.* **716**, 189–202.

GIANNETTI, F. & LUCHINI, P. 2007 Structural sensitivity of the first instability of the cylinder wake. *J. Fluid Mech.* **581**, 167–197.

GIKADI, J., FÖLLER, S. & SATTELMAYER, T. 2014 Impact of turbulence on the prediction of linear aeroacoustic interactions: acoustic response of a turbulent shear layer. *J. Sound Vib.* **333**, 6548–6559.

GRAF, H. R. & ZIADA, S. 2010 Excitation source of a side-branch shear layer. *J. Sound Vib.* **329**, 2825–2842.

GUDMUNDSSON, K. & COLONIUS, T. 2011 Instability wave models for the near-field fluctuations of turbulent jets. *J. Fluid Mech.* **689**, 97–128.

HECHT, F. 2012 New development in FreeFem++. *J. Numer. Maths* **20** (3–4), 251–265.

HILL, D. C. 1992 A theoretical approach for analyzing the restabilization of wakes. *AIAA Paper* 92-0067.

HOWE, M. S. 1980 The dissipation of sound at an edge. *J. Sound Vib.* **70** (3), 407–411.

HWANG, Y. & COSSU, C. 2010 Amplification of coherent streaks in the turbulent Couette flow: an input–output analysis at low Reynolds number. *J. Fluid Mech.* **643**, 333–348.

IUNGO, G. V., VIOLA, F., CAMARRI, S., PORTÉ-AGEL, F. & GALLAIRE, F. 2013 Linear stability analysis of wind turbine wakes performed on wind tunnel measurements. *J. Fluid Mech.* **737**, 499–526.

KITSIOS, V., CORDIER, L., BONNET, J.-P., OOI, A. & SORIA, J. 2010 Development of a nonlinear eddy-viscosity closure for the triple-decomposition stability analysis of a turbulent channel. *J. Fluid Mech.* **664**, 74–107.

KOOIJMAN, G., GOLLIARD, J. & HIRSCHBERG, A. 2004 Orifice impedance under grazing flow measured with a single microphone method. In *10th AIAA/CEAS Aeroacoustics Conference*. American Institute of Aeronautics and Astronautics.

LUCHINI, P. & BOTTARO, A. 2014 Adjoint equations in stability analysis. *Annu. Rev. Fluid Mech.* **46** (1), 493–517.

MAGRI, L. & JUNIPER, M. P. 2013 Sensitivity analysis of a time-delayed thermo-acoustic system via an adjoint-based approach. *J. Fluid Mech.* **719**, 183–202.

MANTIČ-LUGO, V., ARRATIA, C. & GALLAIRE, F. 2014 Self-consistent mean flow description of the nonlinear saturation of the vortex shedding in the cylinder wake. *Phys. Rev. Lett.* **113**, 084501.

MANTIČ-LUGO, V. & GALLAIRE, F. 2016 Self-consistent model for the saturation mechanism of the response to harmonic forcing in the backward-facing step flow. *J. Fluid Mech.* **793**, 777–797.

MARQUET, O., SIPP, D. & JACQUIN, L. 2008 Sensitivity analysis and passive control of cylinder flow. *J. Fluid Mech.* **615**, 221–252.

MARQUILLIE, M., EHRENSTEIN, U. & LAVAL, J.-P. 2011 Instability of streaks in wall turbulence with adverse pressure gradient. *J. Fluid Mech.* **681**, 205–240.

MCKEON, B. J., SHARMA, A. S. & JACOBI, I. 2013 Experimental manipulation of wall turbulence: a systems approach. *Phys. Fluids* **25** (3), 031301.

MELIGA, P. 2017 Harmonics generation and the mechanics of saturation in flow over an open cavity: a second-order self-consistent description. *J. Fluid Mech.* **826**, 503–521.

MELIGA, P., PUJALS, G. & SERRE, E. 2012 Sensitivity of 2-D turbulent flow past a D-shaped cylinder using global stability. *Phys. Fluids* **24** (6), 061701.

MELIGA, P., SIPP, D. & CHOMAZ, J.-M. 2010 Open-loop control of compressible afterbody flows using adjoint methods. *Phys. Fluids* **22** (5), 054109.

METTOT, C., SIPP, D. & BÉZARD, H. 2014 Quasi-laminar stability and sensitivity analyses for turbulent flows: prediction of low-frequency unsteadiness and passive control. *Phys. Fluids* **26** (4).

MORRIS, S. C. 2011 Shear-layer instabilities: particle image velocimetry measurements and implications for acoustics. *Annu. Rev. Fluid Mech.* **43** (1), 529–550.

NAKIBOĞLU, G., MANDERS, H. B. M. & HIRSCHBERG, A. 2012 Aeroacoustic power generated by a compact axysymmetric cavity: prediction of self-sustained oscillation and influence of the depth. *J. Fluid Mech.* **703**, 163–191.

OBERLEITHNER, K., PASCHEREIT, C. O. & WYGNANSKI, I. 2014 On the impact of swirl on the growth of coherent structures. *J. Fluid Mech.* **741**, 156–199.

OBERLEITHNER, K., SCHIMEK, S. & PASCHEREIT, C. O. 2015 Shear flow instabilities in swirl-stabilized combustors and their impact on the amplitude dependent flame response: a linear stability analysis. *Combust. Flame* **162** (1), 86–99.

PIOT, E., CASALIS, G., MULLER, F. & BAILLY, C. 2006 Investigation of the PSE approach for subsonic and supersonic hot jets. Detailed comparisons with LES and linearized Euler equations results. *Intl J. Aeroacoust.* **5** (4), 361–393.

POINSOT, T., YIP, B., VEYNANTE, D., TROUVÉ, A., SAMANIEGO, J. M. & CANDEL, S. 1992 Active control: an investigation method for combustion instabilities. *J. Phys.* III **2** (7), 1331–1357.

POPE, S. B. 2000 *Turbulent Flows*. Cambridge University Press.

PUJALS, G., GARCÍA-VILLALBA, M., COSSU, C. & DEPARDON, S. 2009 A note on optimal transient growth in turbulent channel flows. *Phys. Fluids* **21** (1), 015109.

QADRI, U. A. & SCHMID, P. J. 2017 Frequency selection mechanisms in the flow of a laminar boundary layer over a shallow cavity. *Phys. Rev. Fluids* **2**, 013902.

REYNOLDS, W. C. & HUSSAIN, A. K. M. F. 1972 The mechanics of an organized wave in turbulent shear flow. Part 3. Theoretical models and comparisons with experiments. *J. Fluid Mech.* **54**, 263–288.

ROCKWELL, D. 1983 Oscillations of impinging shear layers. *AIAA J.* **21** (5), 645–664.

ROCKWELL, D. & NAUDASCHER, E. 1978 Review – self-sustaining oscillations of flow past cavities. *J. Fluids Engng* **100** (2), 152–165.

ROCKWELL, D. & NAUDASCHER, E. 1979 Self-sustained oscillations of impinging free shear layers. *Annu. Rev. Fluid Mech.* **11** (1), 67–94.

ROSSITER, J. E. 1964 Wind tunnel experiments on the flow over rectangular cavities at subsonic and transonic speeds. *Tech. Rep.* Aeronautical Research Council Reports and Memoranda.

ROWLEY, C. W. & WILLIAMS, D. R. 2006 Dynamics and control of high-Reynolds-number flow over open cavities. *Annu. Rev. Fluid Mech.* **38**, 251–276.

SIPP, D. & LEBEDEV, A. 2007 Global stability of base and mean flows: a general approach and its applications to cylinder and open cavity flows. *J. Fluid Mech.* **593**, 333–358.

TAM, C. K. W. & BLOCK, P. J. W. 1978 On the tones and pressure oscillations induced by flow over rectangular cavities. *J. Fluid Mech.* **89** (2), 373–399.

TAMMISOLA, O. & JUNIPER, M. P. 2016 Coherent structures in a swirl injector at $Re = 4800$ by nonlinear simulations and linear global modes. *J. Fluid Mech.* **792**, 620–657.

TONON, D., HIRSCHBERG, A., GOLLIARD, J. & ZIADA, S. 2011 Aeroacoustics of pipe systems with closed branches. *Intl J. Aeroacoust.* **10** (2–3), 201–275.

TURTON, S. E., TUCKERMAN, L. S. & BARKLEY, D. 2015 Prediction of frequencies in thermosolutal convection from mean flows. *Phys. Rev.* E **91**, 043009.

VIOLA, F., IUNGO, G. V., CAMARRI, S., PORTÉ-AGEL, F. & GALLAIRE, F. 2014 Prediction of the hub vortex instability in a wind turbine wake: stability analysis with eddy-viscosity models calibrated on wind tunnel data. *J. Fluid Mech.* **750**, R1.